Morphological and Histological Examination

The degree of lower hind limb necrosis and thigh muscle necrosis was macroscopically evaluated on graded morphological scales (grade 1 to 3) for peripheral tissue damage and muscle necrosis area of the adductor, semimembranous, and medial large muscles. Capillary density of the ischemic hind limb was evaluated by alkaline phosphatase staining, as reported previously.[17] A total of 10 different fields from three different sections were randomly selected, and the number of capillaries was counted under a ×40 objective. Capillary density was expressed as the mean number of capillaries per square millimeter. The number of myofibers in each field was also examined and the capillary/muscle fiber ratio calculated.

Radioimmunoassay for Human AM

Human AM production was examined 1, 2, and 4 weeks after gene transfer in the naked AM group, AM-gelatin group, and control group (n=5 each). The muscles were harvested for radioimmunoassay and immunohistochemical examination. Immunoreactive human AM level in rabbit muscles was determined by immunoradiometric assay with the use of a specific kit (Shionogi Co, Ltd).[19] Tissue content of vascular endothelial growth factor (VEGF) was examined by ELISA kit (R&D systems).

Immunohistochemistry for Human AM, Ki67 Antigen, and Phosphorylated Akt

Immunohistochemical studies were performed on formalin-fixed, paraffin-embedded 4-μm sections of ischemic thigh muscles 7 days after gene transfer. To elucidate AM expression after gene therapy, immunohistochemistry for human AM was performed with the use of a monoclonal antibody recognizing AM-(12–25) (1:100), as reported previously.[20] To evaluate the proliferative potential of AM, tissue sections were stained for Ki67, a marker for cell proliferation, with the use of monoclonal anti-Ki67 antibody (1:100) (DAKO). AM has recently been shown to promote proliferation of vascular endothelial cells at least in part through the PI3k/Akt pathway.[21] Thus, immunohistochemistry for phosphorylated Akt was performed with mouse monoclonal anti-phosphorylated Akt antibody (1:100) (Cell Signaling Technology).

Western Blot Analysis

To identify Akt phosphorylation in ischemic muscles after AM gene transfer, Western blotting was performed with the use of a commercially available kit (PhosphoPlus Akt [Ser473] Antibody Kit, Cell Signaling Technology). Ischemic muscles in the 3 groups were obtained 7 days after AM gene transfer. These samples were homogenized on ice in 0.1% Tween 20 homogenization buffer with a protease inhibitor (Complete, Roche). After centrifugation for 20 minutes at 4°C, the supernatant was used for Western blot analysis. The 50 μg of protein was transferred into sample buffer, loaded on 7.5% SDS-polyacrylamide gel, and blotted onto nitrocellulose membrane through the use of a wet blotting system. After blocking for 60 minutes, the membranes were incubated with primary antibodies (1:500) at 4°C overnight. The membranes were then incubated with secondary antibodies, which were conjugated with horseradish peroxidase (Cell Signaling Technology), at a final dilution of 1:2000. Signals were detected through the use of LumiGLO chemiluminescence reagents (Cell Signaling Technology).

Statistical Analysis

All results are expressed as mean±SEM. Statistical significance was evaluated by 1-way ANOVA followed by Fisher's analysis, Scheffe's F analysis, or Kruskal-Wallis test. A value of $P<0.05$ was considered statistically significant.

Results

Physiological and Morphological Assessment

Complete resection of the left femoral artery resulted in a similar decrease in calf blood pressure ratio among the 3 groups before the initiation of therapy (day 10) (Figure 2A). However, the calf blood pressure ratio on day 38 was highest in the AM-gelatin groups, followed by the naked AM group and subsequently the control group. The laser Doppler flow in hind limb was highest in the AM-gelatin group, followed by the naked AM group and the control group (Figure 2B). The calf blood pressure ratio and laser Doppler flow 4 weeks after gene transfer did not significantly differ between the control group and Lac Z-gelatin group. Lower hind limb necrosis was minimal in the AM-gelatin group, followed by the naked AM group and the control group (Figure 2C). Thigh muscle necrosis was also minimal in the AM-gelatin group. Similarly, the muscle weight ratio (ischemic/normal) on day 38 was highest in the AM-gelatin group (Table). Neither mean arterial pressure nor heart rate significantly differed among the 3 groups.

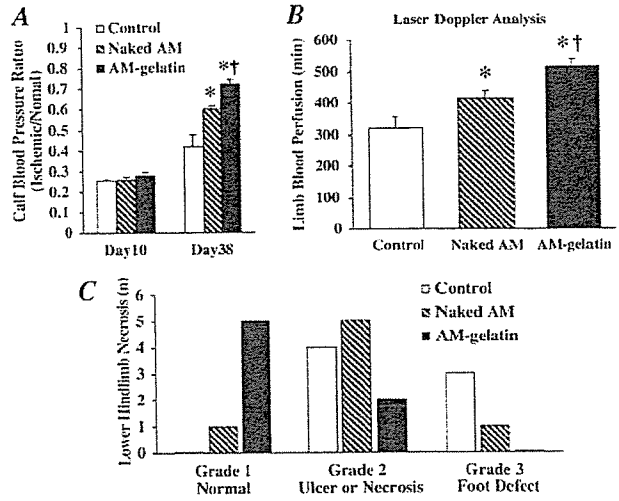

Figure 2. A, Calf blood pressure ratio (ischemic/normal hind limb) before (on day 10) and after (on day 38) gene transfer. B, Measurement of laser Doppler flow on day 38. Data are mean±SEM. *$P<0.05$ vs control group; †$P<0.05$ vs naked AM group. C, Number of cases of each grade of lower hind limb necrosis on day 38. Lower hind limb necrosis was minimal in the AM-gelatin group. Number of necrosis or foot defect is statistically significant among the 3 groups ($P<0.05$ by Kruskal-Wallis test).

Angiographic Analysis

Angiograms 4 weeks after gene transfer (day 38) showed the development of collateral arteries in the naked AM and

Physiological Characteristics

	Control	Naked AM	AM-Gelatin
No. of rabbits	7	7	7
Body weight, kg	2.46±0.06	2.65±0.10	3.16±0.09
MAP, mm Hg	112±3	114±3	116±2
HR, beats/min	269±12	253±5	262±7
Muscle weight ratio	0.71±0.03	0.84±0.02*	0.95±0.02*†

MAP indicates mean arterial pressure; HR, heart rate; and muscle weight ratio, ratio of muscle weight in ischemic hind limb to that in nonischemic hind limb. Data are mean SEM.

*$P<0.01$ vs control group; †$P<0.05$ vs naked AM group.

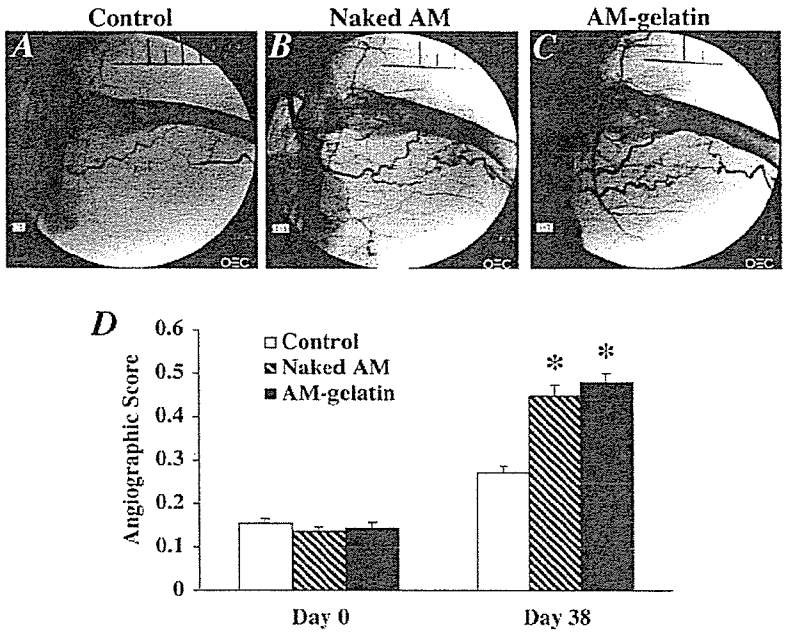

Figure 3. Representative angiograms of control group (A), naked AM group (B), and AM-gelatin group (C) on day 38. Collateral arteries were well developed in the naked AM and AM-gelatin groups. D, Angiographic score on days 0 and 38 in each group. Angiographic score on day 38 was significantly higher in the naked AM and AM-gelatin groups than in the control group. Data are mean±SEM. *$P<0.001$ versus control group.

AM-gelatin groups compared with that in the control group (Figure 3, A through C). Quantitative analysis of collateral vessels demonstrated that the angiographic score in both the naked AM and AM-gelatin groups was significantly higher than that in the control group (Figure 3D). Angiographic score did not significantly differ between the control group and Lac Z-gelatin group.

To examine the development of collateral vessels in an earlier stage, other rabbits (n=4 each) were examined 2 weeks after gene transfer (day 24). Angiograms showed significant collateral development in the naked AM and AM-gelatin groups compared with that in the control group.

Histological Examination

Alkaline phosphatase staining of ischemic hind limb muscle showed marked augmentation of neovascularization in both the naked AM and AM-gelatin groups compared with the control group (Figure 4, A through C). Quantitative analysis demonstrated that capillary density of the ischemic adductor muscle was highest in the AM-gelatin group (Figure 4D). Analysis of the capillary/muscle fiber ratio yielded similar results. Seven days after gene transfer, intense immunostaining for Ki67 was observed in vascular endothelial cells of the naked AM and the AM-gelatin groups (Figure 4, E through G).

AM Expression and Akt Phosphorylation After Gene Transfer

Seven days after gene transfer, modest immunostaining for human AM was observed in the naked AM group, whereas AM immunoreactivity was intense surrounding the gelatin in the AM-gelatin group (Figure 5, A through C). Tissue content of human AM was significantly increased both in the naked AM and the AM-gelatin groups 7 days after gene transfer (Figure 5D). The AM level in the AM-gelatin group was significantly higher that in the naked AM group. Two weeks after gene transfer, AM overexpression was observed only in the AM-gelatin group. The expression of endogenous VEGF and its receptors (Flt-1 and Flk-1) did not differ among the 3 groups (data not shown). Western blot analysis revealed that phosphorylated Akt in ischemic muscles was increased in both the naked AM and AM-gelatin groups 7 days after gene transfer (Figure 5E). Intense immunostaining for phosphory-

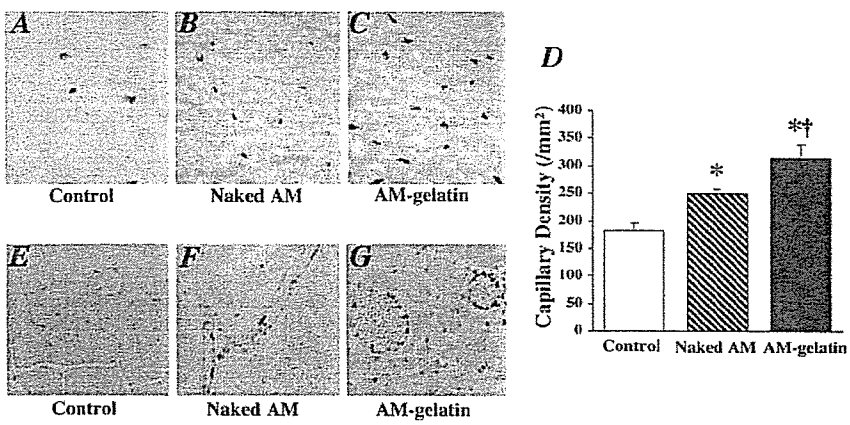

Figure 4. A through C, Representative examples of alkaline phosphatase staining in ischemic hind limb muscles. Magnification ×200. D, Quantitative analysis of capillary density in ischemic hind limb muscles. Data are mean±SEM. *$P<0.05$ vs control group; †$P<0.05$ vs naked AM group. E through G, Immunohistochemical analysis of Ki67 antigen, a marker for cell proliferation. Magnification ×400.

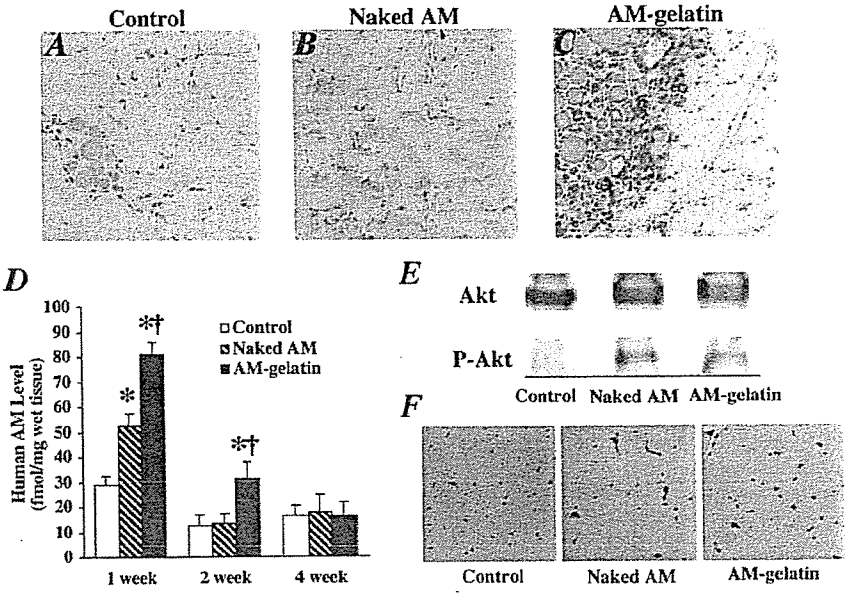

Figure 5. A through C, Immunohistochemistry for human AM 7 days after gene transfer. Intense immunostaining was observed surrounding gelatin in the AM-gelatin group. Magnification ×200. D, Time course of AM production in ischemic muscles after gene transfer. Data are mean±SEM. *$P<0.01$ vs control group; †$P<0.01$ vs naked AM group. E, Western blot analysis for Akt phosphorylation in muscles. F, Immunohistochemical staining for phosphorylated Akt 7 days after gene transfer. Phosphorylated Akt was distributed at least in endothelial cells. Magnification ×400.

lated Akt was observed at least in endothelial cells of the Naked AM and the AM-gelatin groups (Figure 5F).

Discussion

We demonstrated that (1) AM gene transfer induced hemodynamic and angiographic improvements in association with an increase in capillary density in a rabbit model of chronic hind limb ischemia. We also demonstrated that (2) administration of AM DNA-gelatin complexes markedly augmented AM expression and thereby enhanced the therapeutic effects of AM gene transfer.

AM has a variety of effects on the vasculature that include vasodilation,[1,5–7] inhibition of endothelial cell apoptosis,[8,9] and regulation of smooth muscle cell proliferation.[10] However, whether AM has angiogenic potential has remained unknown. In the present study, intramuscular administration of naked AM DNA augmented AM production in skeletal muscles, as indicated by increased tissue content and significant immunostaining of AM. As a result, AM gene transfer increased hind limb perfusion and ameliorated lower hind limb and thigh muscle necrosis in a rabbit model of hind limb ischemia. AM gene transfer may protect the ischemic hind limb partly by improving the blood flow in the ischemic hind limb because AM is originally identified as a potent vasodilating peptide.[1] Nevertheless, angiographic collateral development and high capillary density were observed in ischemic muscles after AM gene transfer. Ki67, a marker for cell proliferation, was detected in endothelial cells of microvessels after AM gene transfer. These results suggest that AM overproduction resulting from gene transfer may induce angiogenesis in a rabbit model of hind limb ischemia. Recent studies using AM gene knockout mice have shown that AM is essential for development of the vasculature during embryogenesis.[11–13] These studies support our results that AM may be an angiogenic factor. VEGF is known to induce angiogenesis and to regulate endothelial cell survival through the phosphatidylinositol 3-kinase (PI3K)/Akt pathway.[22] Thus, the PI3K/Akt pathway is considered to regulate multiple critical steps in angiogenesis, including endothelial cell survival, proliferation, migration, and capillary-like structure formation.[14] A recent study has reported that AM promotes proliferation and migration of human umbilical vein endothelial cells at least in part through the PI3K/Akt pathway.[21] The present study demonstrated that phosphorylated Akt is increased at least in endothelial cells after AM gene transfer. AM gene transfer did not influence endogenous VEGF and its receptors. Taken together, it is interesting to speculate that AM may directly induce angiogenesis through the PI3K/Akt pathway.

In the present study, we used positively charged biodegradable gelatin as a nonviral vector. We have shown that basic fibroblast growth factor (bFGF) is ionically linked with gelatin, which enhances the angiogenic effects of bFGF by delaying protein degradation.[15] Thus, biodegradable gelatin has been used as a carrier of protein. However, little information is available regarding the therapeutic potential of gelatin as a nonviral vector for gene transfer. In the present study, we demonstrated that RITC-labeled AM DNA was incorporated into positively charged gelatin. In addition, intramuscular administration of AM DNA-gelatin complexes strongly enhanced AM production compared with that of naked AM DNA. These results suggest that biodegradable gelatin may serve as a vector for gene transfer. In fact, AM DNA-gelatin complexes induced more potent angiogenic effects in a rabbit model of hind limb ischemia than naked AM DNA, as evidenced by significant increases in histological capillary density, calf blood pressure ratio, laser Doppler flow, and muscle weight ratio and a decrease in necrosis of lower hind limb and thigh muscles. These results suggest that the use of biodegradable gelatin as a nonviral vector augments AM expression and enhances AM-induced angiogenic effects. The angiogenic effects of AM-gelatin complexes were comparable to those of bFGF-gelatin complexes (data not shown). AM DNA-gelatin complexes were distributed mainly in connective tissues. We have recently demonstrated that gelatin-DNA complex is readily phagocytosed by mac-

rophages, monocytes, endothelial progenitor cells, and so on, resulting in gene expression within these phagocytes.[23,24] These findings raise the possibility that AM secreted from these cells acts on muscles in a paracrine fashion. Unlike AM production in the naked AM group, AM overexpression in the AM-gelatin group lasted for longer than 2 weeks. Thus, it is interesting to speculate that delaying gene degradation by gelatin may be responsible for the highly efficient gene transfer.

Currently, a highly efficient and safe gene delivery system is needed for gene therapy in humans. The present study demonstrated that the use of gelatin, which is considered to be less biohazardous than viral vectors, enhanced the angiogenic potential of AM DNA. Thus, gelatin-mediated AM gene transfer may be a new therapeutic strategy for the treatment of severe peripheral vascular diseases. However, the initial success of gelatin-mediated AM gene therapy reported here should be confirmed by long-term experiments, and extensive toxicity studies in animals are needed before clinical trials.

Study Limitation

First, histological capillary density, calf blood pressure ratio, and laser Doppler flow were significantly higher in the AM-gelatin group than in the naked AM group. However, the angiographic score did not significantly differ between the two. This discrepancy raises the possibility that conventional angiography may have insufficient resolution to fully visualize the angiogenic microvessels. Second, human AM level was slightly elevated in the control group. This implies that the anti-human AM antibody used in this radioimmunoassay had some cross-reactivity with endogenous rabbit AM. Nevertheless, human AM level in the muscles was highest in the AM-gelatin group within 2 weeks after gene transfer. These results suggest that AM DNA-gelatin complexes induces potent and long-lasting AM production.

Conclusions

Intramuscular administration of AM DNA induced therapeutic angiogenesis in a rabbit model of chronic hind limb ischemia. Furthermore, the use of biodegradable gelatin as a nonviral vector augmented AM expression and thereby enhanced the therapeutic effects of AM gene transfer. Thus, gelatin-mediated AM gene transfer may be a new therapeutic strategy for the treatment of peripheral vascular diseases.

Acknowledgments

This work was supported by a grant from the Japan Cardiovascular Research Foundation. HLSRG-RAMT-nano-001 and -RHGTEFB-genome-005. RGCD13C-1 from MHLW, grants from NEDO, a Grant-in-Aid for Scientific research from MECSST (13470154 and13877114), and the Promotion of Fundamental Studies in Health Science of the Organization for Pharmaceutical Safety and Research (OPSR) of Japan.

References

1. Kitamura K, Kangawa K, Kawamoto M, et al. Adrenomedullin: a novel hypotensive peptide isolated from human pheochromocytoma. *Biochem Biophys Res Commun*. 1993;192:553–560.
2. Sugo S, Minamino N, Kangawa K, et al. Endothelial cells actively synthesize and secrete adrenomedullin. *Biochem Biophys Res Commun*. 1994;201:1160–1166.
3. Sugo S, Minamino N, Shoji H, et al. Production and secretion of adrenomedullin from vascular smooth muscle cells: augmented production by tumor necrosis factor-alpha. *Biochem Biophys Res Commun*. 1994;203:719–726.
4. Kato J, Kitamura K, Kangawa K, et al. Receptors for adrenomedullin in human vascular endothelial cells. *Eur J Pharmacol*. 1995;289:383–385.
5. Shimekake Y, Nagata K, Ohta S, et al. Adrenomedullin stimulates two signal transduction pathways, cAMP accumulation and Ca^{2+} mobilization, in bovine aortic endothelial cells. *J Biol Chem*. 1995;270:4412–4417.
6. Nagaya N, Satoh T, Nishikimi T, et al. Hemodynamic, renal, and hormonal effects of adrenomedullin infusion in patients with congestive heart failure. *Circulation*. 2000;101:498–503.
7. Nishimatsu H, Suzuki E, Nagata D, et al. Adrenomedullin induces endothelium-dependent vasorelaxation via the phosphatidylinositol 3-kinase/Akt-dependent pathway in rat aorta. *Circ Res*. 2001;89:63–70.
8. Kato H, Shichiri M, Marumo F, et al. Adrenomedullin as an autocrine/paracrine apoptosis survival factor for rat endothelial cells. *Endocrinology*. 1997;138:2615–2620.
9. Sata M, Kakoki M, Nagata D, et al. Adrenomedullin and nitric oxide inhibit human endothelial cell apoptosis via a cyclic GMP-independent mechanism. *Hypertension*. 2000;36:83–88.
10. Kano H, Kohno M, Yasunari K, et al. Adrenomedullin as a novel antiproliferative factor of vascular smooth muscle cells. *J Hypertens*. 1996;14:209–213.
11. Shindo T, Kurihara Y, Nishimatsu H, et al. Vascular abnormalities and elevated blood pressure in mice lacking adrenomedullin gene. *Circulation*. 2001;104:1964–1971.
12. Caron KM, Smithies O. Extreme hydrops fetalis and cardiovascular abnormalities in mice lacking a functional adrenomedullin gene. *Proc Natl Acad Sci USA*. 2001;98:615–619.
13. Imai Y, Shindo T, Maemura K, et al. Evidence for the physiological and pathological roles of adrenomedullin from genetic engineering in mice. *Ann N Y Acad Sci*. 2001;947:26–34.
14. Shiojima I, Walsh K. Role of Akt signaling in vascular homeostasis and angiogenesis. *Circ Res*. 2002;90:1243–1250.
15. Tabata Y, Hijikata S, Muniruzzaman M, et al. Neovascularization effect of biodegradable gelatin microspheres incorporating basic fibroblast growth factor. *J Biomater Sci Polym Ed*. 1999;10:79–94.
16. Fukunaka Y, Iwanaga K, Morimoto K, et al. Controlled release of plasmid DNA from cationized gelatin hydrogels based on hydrogel degradation. *J Control Release*. 2002;80:333–343.
17. Takeshita S, Zheng LP, Brogi E, et al. Therapeutic angiogenesis: a single intraarterial bolus of vascular endothelial growth factor augments revascularization in a rabbit ischemic hindlimb model. *J Clin Invest*. 1994;93:662–670.
18. Van Belle E, Witzenbichler B, Chen D, et al. Potentiated angiogenic effect of scatter factor/hepatocyte growth factor via induction of vascular endothelial growth factor. *Circulation*. 1998;97:381–390.
19. Ohta H, Tsuji T, Asai S, et al. A simple immunoradiometric assay for measuring the entire molecules of adrenomedullin in human plasma. *Clin Chim Acta*. 1999;287:B131–B143.
20. Nagaya N, Nishikimi T, Yoshihara F, et al. Cardiac adrenomedullin gene expression and peptide accumulation after acute myocardial infarction in rats. *Am J Physiol Regul Integr Comp Physiol*. 2000;278:R1019–R1026.
21. Miyashita K, Itoh H, Sawada N, et al. Adrenomedullin promotes proliferation and migration of cultured endothelial cells. *Hypertens Res*. 2003;26:S93–S98.
22. Jiang BH, Zheng JZ, Aoki M, et al. Phosphatidylinositol 3-kinase signaling mediates angiogenesis and expression of vascular endothelial growth factor in endothelial cells. *Proc Natl Acad Sci USA*. 2000;97:1749–1753.
23. Tabata Y, Ikada Y. Macrophage activation through phagocytosis of muramyl dipeptide encapsulated in gelatin microspheres. *J Pharm Pharmacol*. 1987;39:698–704.
24. Nagaya N, Kangawa K, Kanda M, et al. Hybrid cell-gene therapy for pulmonary hypertension based on phagocytosing action of endothelial progenitor cells. *Circulation*. 2003;108:889–895.

THE JOURNAL OF BIOLOGICAL CHEMISTRY
Vol. 279, No. 15, Issue of April 9, pp. 14929–14936, 2004
Printed in U.S.A.

A Novel Actin Bundling/Filopodium-forming Domain Conserved in Insulin Receptor Tyrosine Kinase Substrate p53 and Missing in Metastasis Protein*[S]

Received for publication, August 25, 2003, and in revised form, December 26, 2003
Published, JBC Papers in Press, January 29, 2004, DOI 10.1074/jbc.M309408200

Akiko Yamagishi, Michitaka Masuda‡, Takashi Ohki, Hirofumi Onishi, and Naoki Mochizuki

From the Department of Structural Analysis, National Cardiovascular Center Research Institute, 5-7-1 Fujishiro-dai, Suita, Osaka 565-8565, Japan

Insulin receptor tyrosine kinase substrate p53 (IRSp53) has been identified as an SH3 domain-containing adaptor that links Rac1 with a Wiskott-Aldrich syndrome family verprolin-homologous protein 2 (WAVE2) to induce lamellipodia or Cdc42 with Mena to induce filopodia. The recruitment of these SH3-binding partners by IRSp53 is thought to be crucial for F-actin rearrangements. Here, we show that the N-terminal predicted helical stretch of 250 amino acids of IRSp53 is an evolutionarily conserved F-actin bundling domain involved in filopodium formation. Five proteins including IRSp53 and missing in metastasis (MIM) protein share this unique domain and are highly conserved in vertebrates. We named the conserved domain IRSp53/MIM homology domain (IMD). The IMD has domain relatives in invertebrates but does not show obvious homology to any known actin interacting proteins. The IMD alone, derived from either IRSp53 or MIM, induced filopodia in HeLa cells and the formation of tightly packed parallel F-actin bundles *in vitro*. These results suggest that IRSp53 and MIM belong to a novel actin bundling protein family. Furthermore, we found that filopodium-inducing IMD activity in the full-length IRSp53 was regulated by active Cdc42 and Rac1. The SH3 domain was not necessary for IMD-induced filopodium formation. Our results indicate that IRSp53, when activated by small GTPases, participates in F-actin reorganization not only in an SH3-dependent manner but also in a manner dependent on the activity of the IMD.

Insulin receptor tyrosine kinase substrate p53 (IRSp53),[1] also known as brain-specific angiogenesis inhibitor 1-associated protein 2, is a multifunctional adaptor protein enriched in the central nervous system (1–3). The protein contains a unique N-terminal 250-amino acid stretch, a half-Cdc42/Rac interactive binding (CRIB) motif, a proline-rich domain, a Src homology 3 (SH3) domain, and a WW domain-binding motif (WWB). IRSp53 is directly regulated by Rho family small GTPases Rac1 and Cdc42 and provides a molecular link between these GTPases and the actin cytoskeleton regulators Wiskott-Aldrich syndrome protein (WASP) family verprolin homologous protein 2 (WAVE2) and mammalian enabled (Mena), which are involved in the formation of lamellipodia (4, 5) and filopodia (6, 7). Active Cdc42 binds to the half-CRIB motif (6, 7), whereas Rac1 binds to the unique N-terminal domain (8). The association of Rac1 or Cdc42 is proposed to liberate the C-terminal SH3 domain masked intramolecularly by its N terminus, thereby allowing the SH3 domain to interact with its binding partners (4, 7, 9). Thus, the SH3 domain is thought to be essential for IRSp53-mediated actin reorganization. However, the N-terminal half of IRSp53 lacking the SH3 domain was reported to induce neurite outgrowth in a neuroblastoma cell line (6) and filopodia in B16 melanoma cells (10), suggesting that IRSp53 promotes actin reorganization independently of SH3 domain-mediated intermolecular interactions.

Recently, a novel monomeric actin-binding protein, missing in metastasis protein (MIM), containing a WASP homology 2 (WH2) domain in the C terminus, was reported in human and mouse (11–13) and found to share the unique N-terminal domain with IRSp53 (13). We found that the N-terminal domains of MIM and IRSp53 also share other characteristic features; the predicted secondary structures are almost purely helical (see Ref. 9 for IRSp53), and the estimated isoelectric points are around 9. MIM induces actin cytoskeleton reorganization in cultured cells. This activity is not dependent on the C-terminal half (13), suggesting that the N-terminal half containing the IRSp53 homologous domain plays a key role in actin reorganization.

Here we show that IRSp53 and MIM belong to an evolutionarily related protein family sharing a well conserved N-terminal helical domain (IRSp53/MIM homology domain (IMD)) as a key constituent. We investigated the role of the IMD in actin reorganization. Our results indicate that the IMDs of IRSp53 and MIM induce filopodia in cultured cells and form tightly packed F-actin bundles *in vitro*. The filopodium forming activity of the IMD in full-length IRSp53 is regulated by small GTPases. Thus, upon association with active Rac1 or Cdc42, IRSp53 can induce actin cytoskeleton reorganization by dual mechanisms: the SH3-mediated recruitment of F-actin regulators and the action of the novel actin bundling domain in the N terminus. Both mechanisms may work synergistically or additively in controlling cortical actin dynamics.

* This work was supported in part by grants from the Ministry of Health, Labour and Welfare, from the Organization for Pharmaceutical Safety and Research of Japan, Special Coordination Funds for Promoting Science and Technology from the Ministry of Education, Culture, Sports, Science and Technology, and from the Human Science Foundation of Japan. The costs of publication of this article were defrayed in part by the payment of page charges. This article must therefore be hereby marked "*advertisement*" in accordance with 18 U.S.C. Section 1734 solely to indicate this fact.

[S] The on-line version of this article (available at http://www.jbc.org) contains supplemental data.

‡ To whom correspondence should be addressed. Fax: 81-6-6835-5461; E-mail: masuda61@ri.ncvc.go.jp.

[1] The abbreviations used are: IRSp53, insulin receptor tyrosine kinase substrate p53; CRIB, Cdc42/Rac interactive binding; MIM, missing in metastasis protein; SH3, Src homology 3; WWB, WW domain-binding motif; WASP, Wiskott-Aldrich syndrome protein; WH2, WASP homology 2; IMD, IRSp53/MIM homology domain; GFP, green fluorescent protein; GST, glutathione *S*-transferase; IRTKS, insulin receptor tyrosine kinase substrate; aa, amino acids.

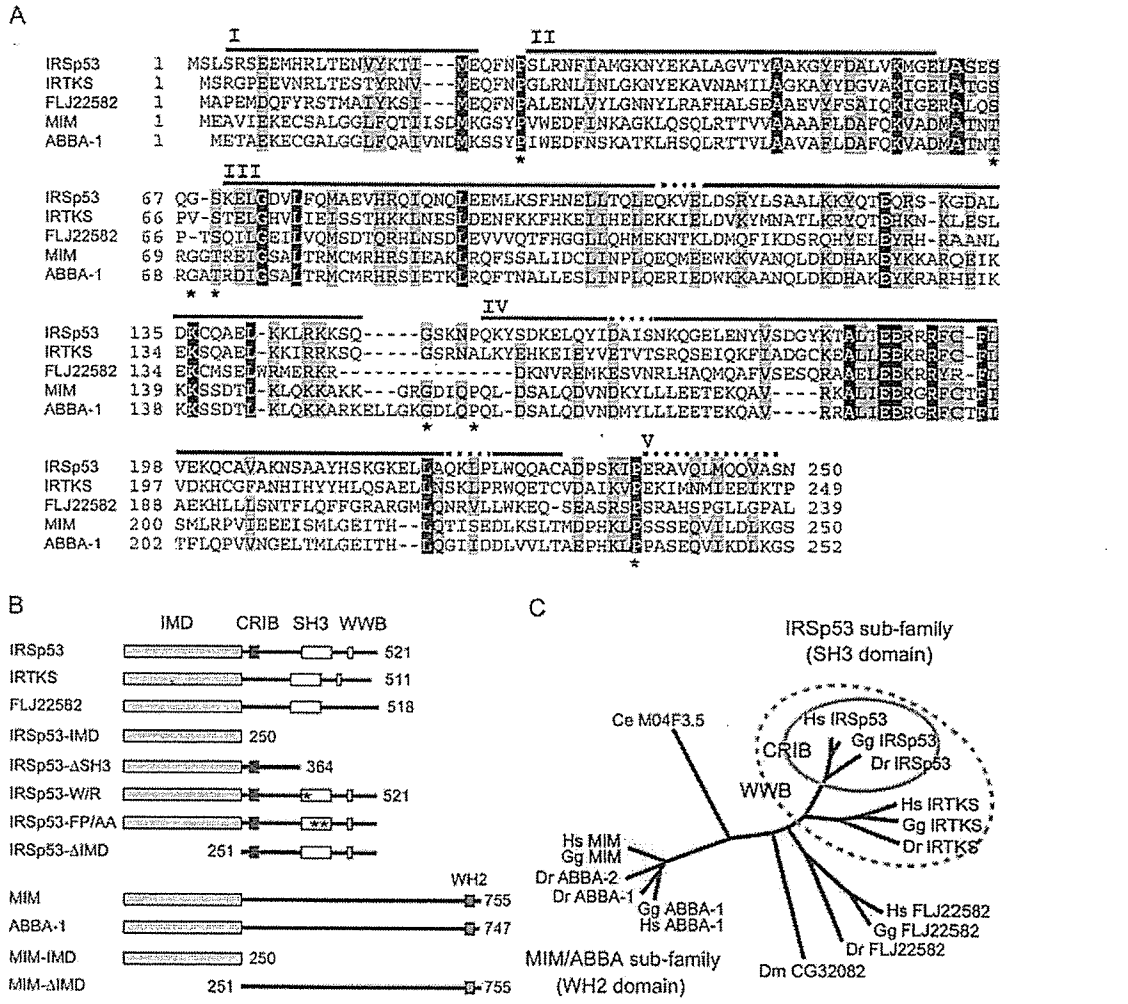

FIG. 1. **The N-terminal helical domains of IRSp53 and MIM are evolutionarily conserved.** *A*, amino acid sequence alignment of the N terminus of known human proteins containing the IMD. The areas where all of the residues are identical are shown in *black*; highly conserved residues are *dark gray*; weakly conserved residues are *light gray*. The *numbered lines* on the sequence show the predicted helical stretches of IRSp53. The *asterisks* show conserved helix-breaking residues. *B*, schematic representation of the domain composition of human proteins containing the IMD. IRSp53 contains a half-CRIB motif (*CRIB*), an SH3 domain (*SH3*), and a WWB. IRTKS lacks CRIB, whereas FLJ22582 lacks both CRIB and WWB. MIM and ABBA-1 each contains a WH2 domain in the C terminus. Truncated fragments of IRSp53 and MIM used in this study are also shown. The positions of mutation in the SH3 domain are indicated by *asterisks*. *C*, unrooted tree of IMDs based on ClustalW alignment. Species used: human (*Hs*), chicken (*Gg*), zebra fish (*Dr*), *D. melanogaster* (*Dm*), and *C. elegans* (*Ce*). Members containing a WWB and a half-CRIB motif are encircled by *dotted circles* and *continuous circles*, respectively. See supplemental Fig. 6 for a full version of the alignment, which was further modified to improve the alignment in the N termini and to match with the predicted helical structures.

EXPERIMENTAL PROCEDURES

Data Base Search—Proteins homologous to IRSp53 and MIM were identified in the GenBank™ data base using BLAST on the National Center for Biotechnology Information web site and on the GenomeNet web site. The details of sequences thus retrieved are described in the supplemental data. The Clustalw engine at the GenomeNet Web site was used to align amino acid sequences and to construct phylogenetic trees. The secondary structures of proteins were predicted by 3D-PSSM (14).

Plasmids—The IRSp53 expression vector pEF-BOS-Myc-IRSp53 (human isoform 1) was kindly donated by Dr. Miki (4). cDNAs encoding full-length IRSp53 (amino acids (aa) 1–521), IRSp53-ΔSH3 (aa 1–364), IRSp53-IMD (aa 1–250), and IRSp53-ΔIMD (aa 251–521) (see Fig. 1*B*) were amplified by PCR and inserted into pEGFP-C1 (Clontech), pCXN2-FLAG (15), and pGEX-4T3 or 6P3 (Amersham Biosciences) vectors. The DNA fragments encoding IRSp53 where Arg was substituted for Trp^{413} or Ala for both Phe^{427} and Pro^{428} in the SH3 domain, hereafter referred to as IRSp53-W/R or IRSp53-FP/AA, were amplified by PCR and ligated into pEGFP-C1. cDNA of Rac1V12, Rac1N17, Cdc42V12, or Cdc42N17 was subcloned into pIRM21, an expression vector expressing FLAG-tagged protein and internal ribosomal entry site-driven dsFP593 (16). A cDNA clone encoding the N-terminal fragment (aa 1–430) of human MIM was obtained by PCR from a human brain cDNA library (Clontech). The cDNA encoding C-terminal MIM (aa 400–755, KIAA0429) was obtained from the Kazusa DNA Research Institute. The full-length MIM cDNA was amplified through overlap PCR using these N- and C-terminal cDNAs as templates. The cDNAs encoding the full-length human MIM (aa 1–755), MIM-IMD (aa 1–250), and MIM-ΔIMD (aa 251–755) were inserted into pEGFP-C1, pCXN2-FLAG, and pGEX-4T3 or 6P3 vectors.

Cells and Transfection—HeLa cells and 293T cells were cultured in Dulbecco's modified Eagle's medium containing 10% fetal bovine serum and 2 mM L-glutamine. HeLa cells and 293T cells were transfected using LipofectAMINE (Invitrogen) according to the manufacturer's protocol.

Antibodies and Immunofluorescence Analysis—Rhodamine-conjugated phalloidin and Alexa546-conjugated anti-mouse IgG were purchased from Molecular Probes (Eugene, OR); anti-FLAG M2 antibody was from Sigma-Aldrich. HeLa cells transfected with the plasmids indicated in the figures and cultured for 15–18 h were fixed with 2% formaldehyde in phosphate-buffered saline and permeabilized with 0.1% Triton X-100 in phosphate-buffered saline. The cells transfected with plasmids expressing GFP-tagged proteins were counterstained with rhodamine-phalloidin. The cells transfected with both GFP-tagged protein-expressing vectors and FLAG-tagged small GTPase-expressing

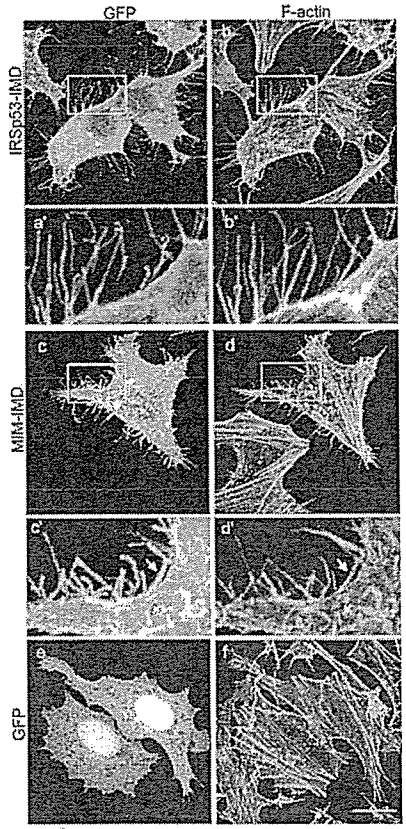

FIG. 2. **The IMDs of IRSp53 and MIM induce filopodia.** HeLa cells were transfected with the GFP-tagged IMD of IRSp53 (*panels a* and *b*), that of MIM (*panels c* and *d*), or GFP alone (*panels e* and *f*). The GFP signal (*left column*) and F-actin visualized with rhodamine-phalloidin (*right column*) are shown. *panels a'*, *b'*, *c'*, and *d'* are enlarged micrographs of rectangular areas of the corresponding figures. The *arrows* in *c'* and *d'* show accumulation of MIM-IMD in filopodium/microvillus-like protrusions. *Scale bar*, 20 μm. All analyses of cellular phenotypes in this study were based on observations of cells expressing moderate levels of GFP-tagged IRSp53, MIM, or their fragments. High expressers often showed a dendritic phenotype with severe retraction of the cell body and thus were not used for the analyses.

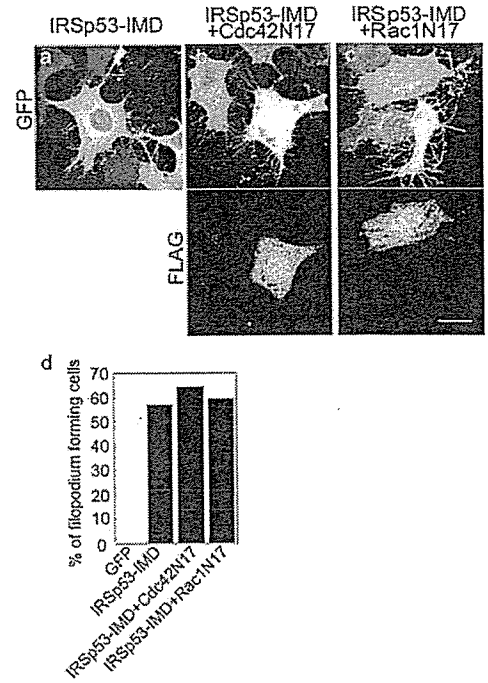

FIG. 3. **The IRSp53-IMD induces filopodia independently of small GTPases.** HeLa cells expressing the GFP-fused IRSp53-IMD (*panels a–c*). The cells were co-transfected with FLAG-tagged dominant negative Cdc42N17 (*panel b*) or Rac1N17 (*panel c*). The *upper row* shows GFP signals, and the *lower row* shows Cdc42N17 (*panel b*) or Rac1N17 (*panel c*) expression detected by FLAG tag. *Scale bar*, 20 μm. The bar graph in *panel d* shows the frequency of cells developing numerous filopodia in a typical experiment. More than 100 cells were analyzed for each data point. Cells expressing both GFP and FLAG-tagged proteins were analyzed.

vectors were immunostained with anti-FLAG M2 antibody followed by an Alexa546-conjugated anti-mouse IgG. Fluorescence images were obtained using a confocal microscope (BX50WI, Fluoview, Olympus, Tokyo, Japan) with a water immersion objective lens (LUMPlanFl 60×, 0.90 W). To show the entire cell morphology in detail, all of the cell images shown were extended focus images reconstructed from a series of optical sections taken at 0.2–0.3-μm intervals.

F-actin Binding and Bundling Assays—F-actin was prepared from rabbit skeletal muscle as described (17). Glutathione *S*-transferase (GST) fusion proteins of various fragments of IRSp53 and MIM (see Fig. 1*B*) were expressed in BL21-Star (DE3) cells (Invitrogen), purified using glutathione-Sepharose (Amersham Biosciences), and then buffer-exchanged into F buffer (25 mM Hepes, pH 7.5, 100 mM KCl, 0.2 mM $CaCl_2$, 2 mM $MgCl_2$, 2 mM EGTA, 0.2 mM ATP, 1 mM dithiothreitol) containing 0.1% $C_{12}E_8$ (Nikko Chemicals, Tokyo, Japan). For binding assays, purified GST-fused fragments were clarified by centrifugation at 400,000 × *g* for 15 min to remove any aggregates, mixed with F-actin in the F buffer, and incubated for 30 min on ice. The final concentration of the GST fusions and F-actin were 1.2 and 5 μM (as for G-actin), respectively. The mixture was then centrifuged as above, and equal aliquots of the supernatant and the pellet were analyzed by SDS-PAGE followed by Coomassie Blue staining. For quantitative analysis of F-actin binding and bundling, the IMDs were cleaved out from the GST fusions expressed by pGEX-6P3 vectors using PreScission Protease (Amersham Biosciences) and further purified by cation exchange chromatography (Resource S; Amersham Biosciences). To quantify F-actin binding, increasing amounts of F-actin were incubated with 2 μM IRSp53-IMD or MIM-IMD in the F buffer for 3 h at room temperature. The samples were then centrifuged and analyzed as above. The protein bands were quantified by densitometry (Personal Densitometer SI; Amersham Biosciences). For quantitative bundling assay, increasing amounts of the IMDs were incubated with 1 μM F-actin in the F buffer for 1 h at room temperature. The supernatant and the pellet were separated by low speed centrifugation (10,000 × *g* for 30 min) and analyzed as above.

Observation of Actin Bundles—For fluorescence microscope observation, a fixed concentration of F-actin (final concentration, 1.2 μM) was mixed with variable concentrations of the GST-fused fragments (0.24 to 12 μM). After incubation for 30 min on ice in F buffer, F-actin was stained with rhodamine-phalloidin for 15 min on ice. The mixtures were applied to poly-L-lysine-coated glass coverslips and incubated for 20 min at room temperature. The adherent material was washed with F buffer and observed with the confocal laser scanning microscope using an oil immersion objective lens (PlanApo 60×, 1.40 oil). For negative staining of actin filaments and bundles, the rhodamine-phalloidin-stained specimens described above were diluted 10 times with F buffer, placed onto a carbon-coated mesh, and stained with 2% uranyl acetate. For observation of thin sectioned specimens, actin bundles formed after incubation for 1 h on ice were packed by centrifugation and fixed in 2.5% glutaraldehyde in 0.1 M cacodylate buffer, pH 7.4, and then sequentially incubated with 0.1% aqueous tannic acid and 0.2% uranyl acetate (18), postfixed in 0.5% aqueous OsO_4, dehydrated, and embedded in Epon 812. Thin sections stained by lead citrate were examined with a CM 120 electron microscope (Philips Electronics, Eindhoven, The Netherlands) equipped with a multiscan cooled charge-coupled device camera (model 791; Gatan, Pleasanton, CA).

Cross-linking of Proteins—One μM of purified IRSp53-IMD, MIM-IMD, and chymotrypsinogen A (Amersham Biosciences) as the control were cross-linked in 0.1 M 2-morpholinoethanesulfonic acid, pH 5.0, at room temperature. The reaction was started by the addition of 4 mM 1-ethyl-3-(3-dimethylaminopropyl) carbodiimide and was stopped by the addition of 50 mM Tris-HCl, pH 8.0, at the time points indicated in Fig. 7*A*.

Immunoprecipitation—293T cells were washed with phosphate-buffered saline and lysed in lysis buffer (100 mM NaCl, 25 mM Hepes, pH

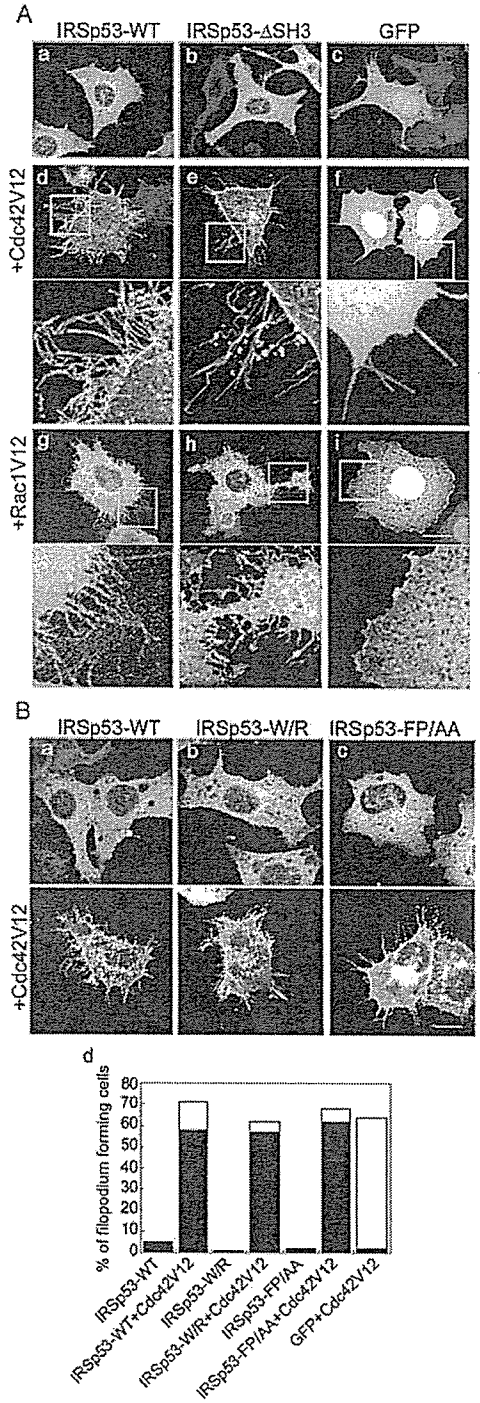

FIG. 4. **The IMD in wild-type IRSp53 is regulated by Cdc42 and Rac1.** *A*, GFP signals of HeLa cells expressing the GFP-tagged full-length IRSp53 (*WT*; *panels a*, *d*, and *g*), the GFP-tagged N-terminal half (*ΔSH3*; *panels b*, *e*, and *h*), or GFP alone (*GFP*; *panels c*, *f*, and *i*). *Panels a–c*, cells without co-transfection. *Panels d–f*, cells co-transfected with Cdc42V12. *Panels g–i*, cells co-transfected with Rac1V12. Enlarged views of the rectangular areas are shown *below*. *Scale bar*, 20 μm. *B*, HeLa cells expressing the GFP-tagged full-length IRSp53 (*WT*; *panel a*), an SH3 mutant with W417R substitution (*W/R*; *panel b*), or another SH3 mutant with F427A/P428A substitutions (*FP/AA*; *panel c*). The *upper row* is without co-transfection, and the *lower row* shows cells co-transfected with the FLAG-tagged active Cdc42. The expression of Cdc42 was detected by FLAG immunostaining (not shown). *Scale bar*, 20 μm. The stacked bar graph in *panel d* shows the frequency of cells presenting the IRSp53+Cdc42 phenotype (*filled bars*) and the Cdc42 phenotype (*open bars*) in a typical experiment. Cells forming numerous, long, wavy, and often branching filopodia (*A*, *panel d* for an example) were counted as the IRSp53+Cdc42 phenotype cells. The cells forming long, straight filopodia (*A*, *panel f* for an example) were counted as the Cdc42 phenotype cells.

7.5, 2 mM $MgCl_2$, 2 mM EGTA, 0.5% Triton X-100, containing protease inhibitor mixture; Roche Applied Science). The lysates were precleared by centrifugation at 100,000 × *g* for 10 min, followed by immunoprecipitation with a rabbit anti-GFP antibody and protein A-Sepharose beads (Amersham Biosciences). The immunoprecipitates were subjected to SDS-PAGE and immunoblotting with antibodies as indicated in Fig. 7*B*. The proteins reacting with primary antibodies were visualized by an enhanced chemiluminescence system (Amersham Biosciences) for detecting peroxidase-conjugated secondary antibodies and analyzed with an LAS-1000 system (Fuji Film, Tokyo, Japan).

RESULTS

The N-terminal Helical Domain Is Evolutionarily Conserved in IRSp53 Family Proteins and MIM Family Proteins—IRSp53 and MIM share the N-terminal stretch of 250 amino acids (22% identical, 18% similar), whereas the remaining parts of the molecules show only marginal similarity. To explore whether this similarity is based on real homology, we searched the GenBank™ data base for proteins having similar sequences. First we found three more genes encoding homologous N-terminal sequences in the human genome: insulin receptor tyrosine kinase substrate (IRTKS), the hypothetical gene *FLJ22582*, and *ABBA-1* (Fig. 1*A*; see the supplemental table for details). IRTKS and FLJ22582 are IRSp53-related proteins containing an SH3 domain in the C-terminal half. However, both of them lack the half-CRIB motif found in IRSp53, and FLJ22582 further lacks the WWB (PPPXY) (Fig. 1*B*). ABBA-1 (GenBank™ accession number AB115770) is a MIM-related protein that possesses a WH2 domain in the C terminus. Further data base searches have shown that each of these five proteins has a putative ortholog in chicken and zebra fish, indicating that they are well conserved through vertebrate evolution (Supplemental Figs. 1–4). As pointed out previously (9, 13), related proteins are also found in invertebrates (*Caenorhabditis elegans* M04F3.5 protein and *Drosophila melanogaster* CG32082 protein). In an amino acid sequence alignment of the N-terminal region of these proteins (Fig. 1*A*), clusters of basic amino acids, proline, glycine, and clusters of hydrophobic amino acids are well conserved. There is a signature sequence of ALXEE(R/K)(R/G)RFCX_{0-1}F(I/L) in the C-terminal half of the stretch. As expected from the number of basic amino acid clusters in this domain, the estimated isoelectric points are highly basic, ranging from 8.5 for human MIM to 9.2 for human FLJ22582.

The identity of the N-terminal domain is further supported by predicted secondary structures. The domains are almost purely helical, 82–87% for the IRSp53-related proteins, 96–100% for MIM-related proteins, and intermediate contents of 89 and 87% for M04F3.5 and CG32082, respectively. Helix-breaking amino acid residues at the four breaking sites of the IRSp53-related proteins are also conserved in MIM/ABBA family proteins (*asterisks* in Fig. 1*A*). Thus, all of these proteins appear to have a common segmentation pattern of helices, helix I–V (Fig. 1*A*). Although human IRSp53 lacks helix V, it is predicted to be present in the chicken ortholog.

A phylogenetic tree (Fig. 1*C*) based on the alignment of the IMDs shows that the vertebrate IRSp53/MIM family is divided into two major groups: the IRSp53 subfamily and the MIM/ABBA subfamily. The putative invertebrate homologs are positioned between them. The tree of the IMDs exactly reflects the hierarchy of domain composition of these proteins. The IRSp53 subfamily members contain an SH3 domain, and the MIM/ABBA subfamily proteins contain a WH2 domain. The

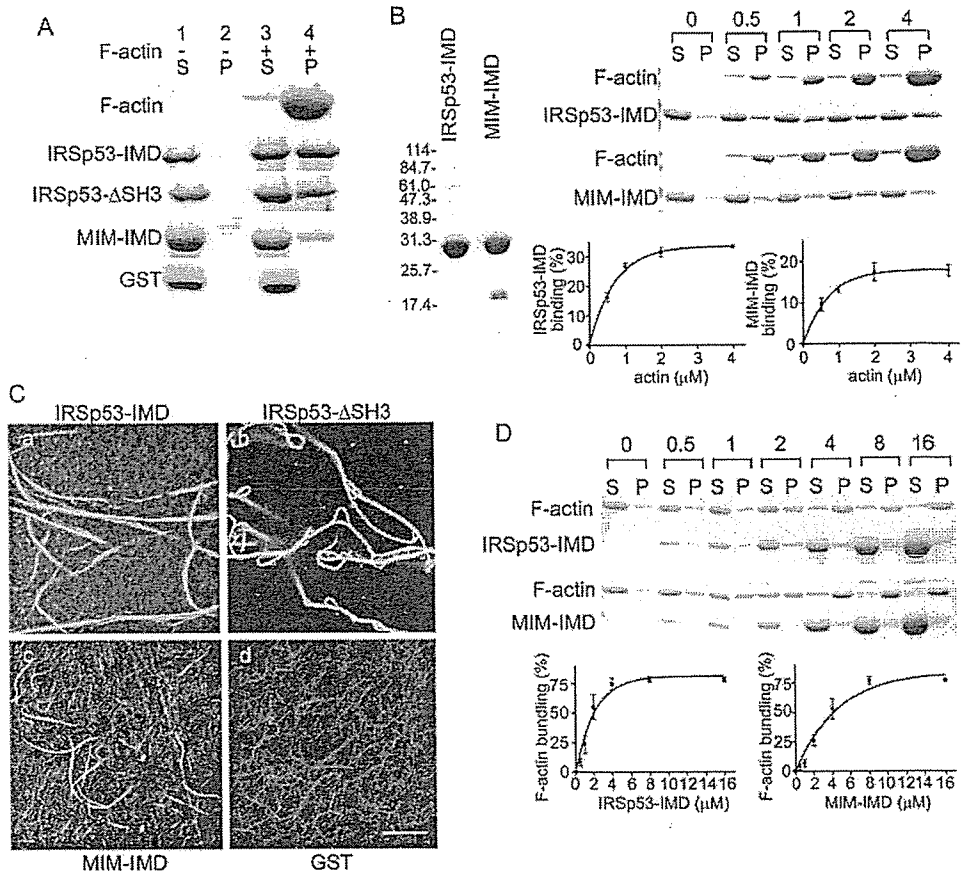

FIG. 5. **F-actin binding/bundling activity of the IRSp53-IMD and MIM-IMD.** *A*, high speed F-actin co-sedimentation assay. 1.2 μM GST-fused IRSp53 fragments (*IRSp53-IMD* and *IRSp53-ΔSH3*), a MIM fragment (*MIM-IMD*), or GST alone (*GST*) were incubated with (+) or without (−) F-actin (5 μM as for G-actin) for 30 min on ice and then ultracentrifuged at 400,000 × *g* for 15 min. Equal aliquots of the supernatant (*S*) and the resuspended pellet (*P*) were analyzed by SDS-PAGE and Coomassie Blue staining. *B*, quantitation of F-actin binding activity of IMDs. Purified tag-free IMDs analyzed by SDS-PAGE are shown in the *left panel*. 2 μM of tag-free IMDs and 0, 0.5, 1, 2, and 4 μM of F-actin were co-sedimented at 400,000 × *g*. The IMD bands stained with Coomassie Blue (*right upper panel* showing a representative data) were quantified by densitometry. The relatively long incubation time used in this experiment caused precipitation of 6–8% of the total IMDs without F-actin. To show the net F-actin binding of the IMDs, the percentage of F-actin-bound IMD was calculated as the percentage recovered in the pellet subtracted by that recovered in the pellet without F-actin. The data shown in the *lower panel* are the means ± S.D. of three independent experiments. *S*, supernatant; *P*, pellet. *C*, visualization of F-actin bundles induced by IMDs. F-actin (1.2 μM) was incubated with 1.2 μM GST-IRSp53-ΔSH3 (*panel a*), 6 μM GST-IRSp53-IMD (*panel b*), 6 μM GST-MIM-IMD (*panel c*), or 1.2 μM GST alone (*panel d*) for 30 min on ice. After staining with rhodamine-phalloidin, actin filaments and bundles were observed under a confocal microscope. *Scale bar*, 10 μm. *D*, quantitation of F-actin bundling activity of IMDs. 0, 0.5, 1, 2, 4, 8, and 16 μM of tag-free IMDs and 1 μM of F-actin were co-sedimented at 10,000 × *g*. 4–10% of total actin was recovered in the pellet in the absence of the IMDs. The percentages of actin in the bundles were quantified as described for Fig. 5*B*. The data shown in the *lower panel* are the means ± S.D. of three independent experiments. *S*, supernatant; *P*, pellet.

vertebrate SH3-containing subfamily is further divided into three groups according to the presence or absence of the WWB and the half-CRIB motif. These data suggest that the IRSp53/MIM family originated from a common ancestor and diverged through evolution. This hypothesis is supported by the fact that IRTKS and FLJ22582 but not M04F3.5 or CG32082 share highly homologous C termini with the MIM/ABBA subfamily members (supplemental Fig. 6). Our analyses suggest the presence of an evolutionarily conserved IRSp53/MIM family and that the IMDs are the key components for the functional roles of proteins belonging to this family.

The IMDs of IRSp53 and MIM Induce Filopodia in HeLa Cells—To explore the functional roles of the IMD, we first examined the morphological effects of ectopic expression of the IRSp53-IMD and the MIM-IMD in HeLa cells. The cells expressing the GFP-tagged IMD of IRSp53 formed numerous long filopodia that were F-actin-rich as demonstrated by rhodamine-phalloidin staining (Fig. 2, *panels a*, *a'*, *b*, and *b'*). The MIM-IMD also induced filopodia, but they were reduced in length (Fig. 2, *panels c*, *c'*, *d*, and *d'*). In addition, MIM-IMD promoted the formation of microvillus-like protrusions on the apical cell surface. IRSp53-IMD and MIM-IMD localized to and occasionally were concentrated in these protrusions (*arrows* in Fig. 2, *panels c'* and *d'*). Both IMDs appeared not to be associated with stress fibers. There were no obvious signs of enhanced lamellipodial activity or disruption of stress fibers in these IMD-expressing cells. GFP used as a negative control did not induce any morphological changes (Fig. 2, *panels e* and *f*). Truncated fragments of IMD, IRSp53-N-IMD (aa 1–161), and IRSp53-C-IMD (aa 105–250) could not stimulate filopodium-formation (data not shown). These data indicate that both IMDs are capable of inducing filopodia in cells. Because IRSp53 and MIM represent the most divergent members of the vertebrate IRSp53/MIM protein family (Fig. 1*C*), the filopodium inducing activity of the IMD is likely to be conserved in all family members.

IMD Does Not Act Upstream of Rac1 or Cdc42 for Filopodium Formation—Actin cytoskeletal reorganization is often a hallmark of Rho family GTPases. Previous reports have shown that Rac1 binds to the N terminus of IRSp53 (8) and Cdc42 binds to

the aa 202–305 fragment containing the half-CRIB motif (6). Therefore, we examined whether Cdc42 or Rac1 activation was involved in IMD-induced filopodium formation. The formation of numerous filopodia induced by IRSp53-IMD was not perturbed by the co-expression of dominant negative Cdc42 or Rac1 (Fig. 3). There was no quantitative difference in the ratio of filopodium forming cells among HeLa cells transfected with IRSp53-IMD alone, those transfected with IRSp53-IMD and Cdc42N17, and those transfected with IRSp53 and Rac1N17 (Fig. 3, *panel d*), suggesting that the IMD itself is not regulated by these small GTPases. This result also excludes the possibility that the domain functions upstream of these small GTPases.

The Filopodium-inducing IMD Activity of Wild-type IRSp53 Is Regulated by Cdc42 and Rac1—The common mechanism of effecter activation by Rho family GTPases appears to be dependent on the disruption of intramolecular autoinhibitory interactions. Cdc42-induced conformational changes have also been demonstrated for the molecule containing a half or semi-CRIB motif, Par6 (19). First we found that GFP-tagged IRSp53-WT or GFP-tagged IRSp53-ΔSH3, when expressed in moderate levels, could not induce filopodia (Fig. 4*A*, *panels a–c*). As reported earlier (7, 10), cells expressing very high amounts of IRSp53 often formed dendritic extensions accompanied with severe retraction of the cell body. As noted in the legend to Fig. 2, these cells were omitted from our analyses. Next, we examined whether the IMD function was regulated by Cdc42 and Rac1 in IRSp53-WT and in IRSp53-ΔSH3 containing the half-CRIB motif. Co-expression of the active Cdc42 with these IRSp53 constructs led to massive formation of wavy filopodia (IRSp53+Cdc42 phenotype as shown in Fig. 4*A*, *panels d* and *e*) that was clearly distinguishable from straight filopodia induced in cells co-expressing GFP and active Cdc42 (Cdc42 phenotype as shown in Fig. 4*A*, *panel f*). A similar level of filopodium induction mixed with Rac1-dependent enhanced lamellipodia activity (Fig. 4*A*, *panel i*) was induced by the co-expression of active Rac1 (Fig. 4*A*, *panels g* and *h*). These results suggest that the SH3 domain is not necessary for IMD-dependent filopodium formation. Our results also suggest that the filopodium-inducing IMD activity in wild-type IRSp53 is regulated by Cdc42 and Rac1. The central region of IRSp53 containing the half-CRIB motif appears to be essential for this regulation, as previously suggested for the regulation of the SH3 domain (7, 9).

To further confirm that the IMD-induced filopodium formation is independent of SH3-binding molecules, we used two nonfunctional SH3 mutants, IRSp53-W/R and IRSp53-FP/AA (7). Both mutants could induce filopodia when expressed with active Cdc42 (Fig. 4*B*). Although active Cdc42 alone induced filopodium formation in the majority of cells (Fig. 4*B*, *panel d*, the blank segment in the stacked bar graph reflecting the Cdc42 phenotype), exaggerated filopodium formation, an indication of IMD activity, occurred only when Cdc42 was co-expressed with IRSp53-WT and IRSp53-SH3 mutants (Fig. 4*B*, *panel d*, the filled segment in the stacked bar graph reflecting the IRSp53+Cdc42 phenotype). Thus, IRSp53 can promote filopodium formation independently of SH3-mediated intermolecular interactions.

In Vitro F-actin Bundling Activity of IMD—The filopodium promoting activity of the IMDs of IRSp53 and MIM in cultured cells led us to examine whether these IMDs have F-actin binding and bundling activity. We examined F-actin binding/bundling activity of the GST-fused IMD and other fragments and also tag-free purified IMDs *in vitro*. As shown in Fig. 5*A*, GST-fused IRSp53-IMD, IRSp53-ΔSH3, and MIM-IMD but not GST were co-sedimented with F-actin in a high speed assay

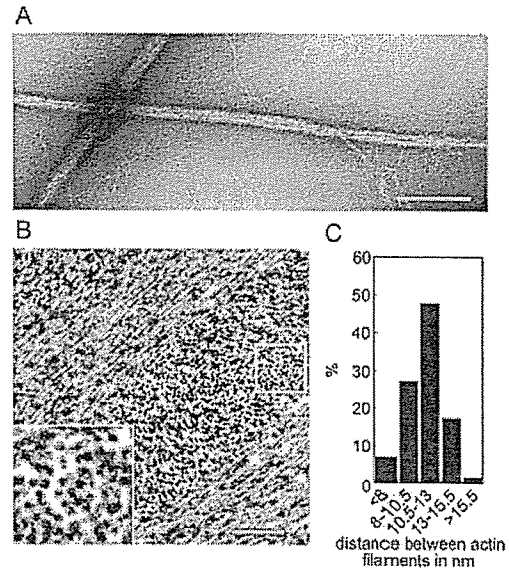

FIG. 6. **Electron micrographs of actin bundles induced by IRSp53.** *A*, negatively stained F-actin bundles induced by GST-fused IRSp53-IMD for 30 min on ice. *Scale bar*, 1 μm. *B*, macroscopically visible tangled threads of actin bundles induced by GST-fused IRSp53-ΔSH3 for 1 h on ice were packed by ultracentrifugation and processed for transmission electron microscopy. Transverse and longitudinal sections of actin bundles ~0.2 μm thick are shown. In a transversely sectioned area (*inset*, enlarged view of the rectangular area), many actin filaments are aligned with a regular center-to-center distance of 11.2 ± 2.0 nm (mean ± S.D., n = 854) as shown in *C*. *Scale bar*, 0.1 μm.

(total binding). To exclude the possible contribution of GST-tag or contaminating bacterial proteins to F-actin binding and bundling, the activities of purified tag-free IMDs (Fig. 5*B*, *left panel*) were examined. In the high speed assays, the IMDs of IRSp53 and MIM bound to F-actin in a concentration-dependent and saturable manner (Fig. 5*B*, *right panel*). The apparent half-maximum concentrations of F-actin for IMD binding were almost the same (0.5 μM), irrespective of the variation between the maximum extents of these IMDs, suggesting that both IMDs have roughly the same affinity to F-actin. Low levels of the maximum extent of bound IMDs, about 30% for IRSp53-IMD and 20% for MIM-IMD, can be explained by improper protein folding of the bacterially made IMDs or their denaturation during the purification process.

The GST fusions capable of F-actin binding induced thick F-actin bundles (Fig. 5*C*). Although GFP-tagged IRSp53-ΔSH3 required activation by Rac1 or Cdc42 for filopodium formation, GST-fused IRSp53-ΔSH3 alone could induce F-actin bundling. It is possible that the bacterially made protein may not be folded properly to form the self-inhibitory conformation. IRSp53-ΔSH3 showed stronger bundling than IRSp53-IMD or MIM-IMD; however, different levels of bundling activity among these proteins may simply reflect differences in stability of these fusion proteins. To quantify the bundling activity, the tag-free IMDs were examined in low speed sedimentation assay (Fig. 5*D*). The bundling activity was concentration-dependent, and most of F-actin could be incorporated into bundles in high concentrations of the IMDs.

The IMD-induced F-actin bundles could be seen under a phase contrast microscope, and their thickness was measured at 0.1–0.2 μm by electron microscope observation of negatively stained materials (Fig. 6*A*). Observation of thin sections of the bundles revealed tight packing of parallel actin filaments in the bundles (Fig. 6*B*). The bundle as a whole was not a paracrystal in which actin filaments were packed into a hexagonal array with a constant spacing of 11.5 nm, as previously described

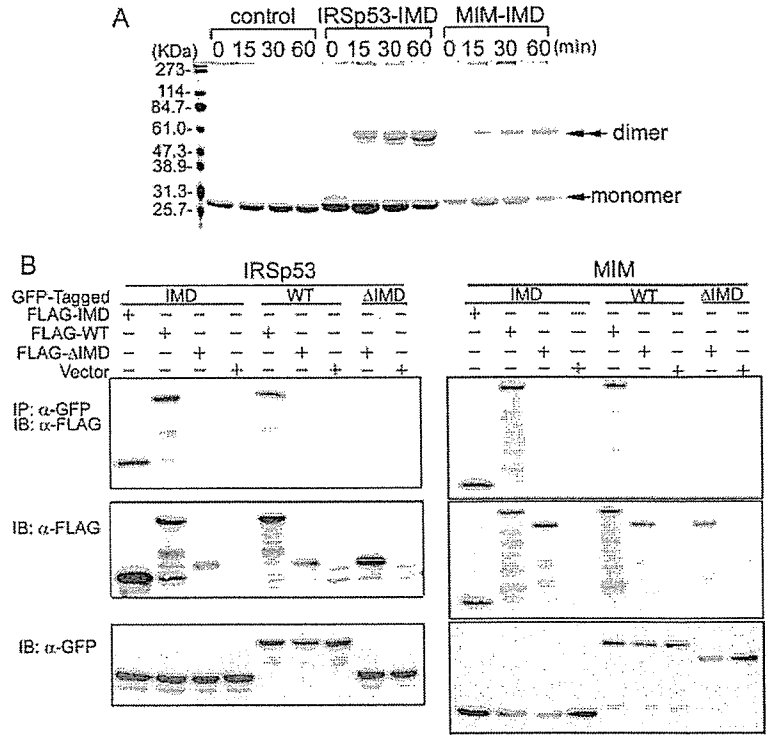

FIG. 7. **Self-association of IMDs.** *A*, analysis of cross-linked IMDs by SDS-PAGE. 1 μM of tag-free IMDs of IRSp53 and MIM were cross-linked with 4 mM 1-ethyl-3-(3-dimethylaminopropyl) carbodiimide for 0, 15, 30, and 60 min. Chymotrypsinogen A was used as a nondimer control. Equal amounts of protein were analyzed by SDS-PAGE followed by Coomassie Blue staining. An *arrow* and *double arrows* point to the monomer and the dimer, respectively. *B*, co-immunoprecipitation assay for self-association of IMDs. GFP-tagged IMD, full-length protein (*WT*), or ΔIMD was co-expressed with FLAG-tagged IMD, WT, ΔIMD, or FLAG-vector alone (*Vector*) in 293T cells. GFP-tagged proteins were immunoprecipitated (*IP*) using anti-GFP antibody and analyzed by immunoblotting (*IB*) with anti-FLAG M2 antibody (*top panel*). Expression levels of FLAG-tagged proteins (*middle panel*) and GFP-tagged proteins (*bottom panel*) are shown by immunoblot analyses of total lysates.

(20). However, actin filaments in the bundles tended to be arranged in a line and partly packed into a hexagonal pattern (Fig. 6*B*, *inset*). The center-to-center distance between neighboring actin filaments aligned in a line was nearly constant and was measured at 11.2 nm in transverse sections (Fig. 6*C*). These observations indicate that IRSp53 acts as a typical parallel actin bundle-forming molecule such as fimbrin and fascin and suggest that the IRSp53/MIM family is a novel actin bundling protein family.

Self-association of IMD—Actin bundling activity requires at least two independent F-actin-binding sites or a combination of one binding site plus a self-association site in an actin bundling domain. The ability of IMDs to form dimers or oligomers was examined by chemical cross-linking using zero-length cross-linker 1-ethyl-3-(3-dimethylaminopropyl) carbodiimide. The apparent molecular mass of the tag-free IMDs in SDS-PAGE was progressively shifted from 30 kDa, which matched to the calculated molecular masses of the IRSp53-IMD (28,972 Da) and MIM-IMD (28,640 Da) including a short linker sequence, to the dimer one of 60 kDa (Fig. 7*A*). Both of the tag-free IMDs were effectively cross-linked into dimers but not into trimers or tetramers. This result suggests that the purified IMDs are present as dimers. Next we examined IMD self-association in cultured cells. The IMDs of IRSp53 or MIM could associate with each other and with the full-length molecule but not with the C-terminal half lacking the IMD (ΔIMD) in co-transfected 293T cells (Fig. 7*B*). Consistent with the IMD-dependent self-association, ΔIMD was not co-immunoprecipitated in any combinations, whereas the full-length IRSp53 and MIM associated with themselves. These results indicate that the IMD is a self-associating domain and suggest that IRSp53 and MIM can be present as dimeric forms in mammalian cells.

DISCUSSION

In this study we show that the N-terminal helical domain, the IMD, identified in IRSp53 and MIM, induces filopodium formation *in vivo* and F-actin bundling *in vitro* and suggests that these domains are conserved in an evolutionarily related protein family, the IRSp53/MIM family. We propose that the IRSp53/MIM family is a novel F-actin bundling protein family that includes invertebrate relatives. Although the family members are largely diverged, each vertebrate member (IRSp53, IRTKS, FLJ22582, MIM, and ABBA) is highly conserved throughout the entire molecule in species ranging from fish to human. They are likely to have a common fundamental function, actin bundle formation, with different mechanisms of regulation.

Parallel actin bundles form the core structure of cellular protrusions such as filopodia, microvilli, and microspikes. These structures are tightly packed, noncontractile bundles cross-linked by a class of F-actin bundling proteins, such as fascin and fimbrin, that determine an ~12-nm spacing between actin filaments (20, 21), and the involvement of such proteins is essential for structure formation (18, 22–24, 26). The other class of bundling proteins, represented by α-actinin, are found in contractile bundles such as stress fibers. There, they cross-link actin filaments with a wide spacing of about 36 nm (27, 28), which allows myosin II to interact with the actin filaments (29). We have shown that the N terminus of IRSp53 induces *in vitro* formation of tightly packed F-actin bundles of 11-nm spacing. The localization of the N-terminal helical domain of IRSp53 and MIM in filopodia with F-actin but not in stress fibers is consistent with the idea that the protein functions in cells as a parallel F-actin bundling protein.

Our present study indicates that SH3-mediated interactions are not always necessary for IRSp53-induced filopodium formation, and this is consistent with a recent report showing that Mena and vasodilator-stimulated phosphoprotein (VASP) are not essential for this process in B16 melanoma cells (10). However, our results neither rule out the Rac1-IRSp53-WAVE2 or Cdc42-IRSp53-Mena pathway nor exclude any contribution of the C-terminal half to IRSp53 induced F-actin rearrangements. The SH3-mediated interactions could contribute to IRSp53 functions by two possible mechanisms. In the first, as in the classical view of IRSp53 function, SH3 ligands play a crucial

role in actin cytoskeleton dynamics, which may additively or synergistically work with the N-terminal IMD. Among these ligands, Ena/VASP family proteins have been reported to have actin bundling activity associated with the Ena/VASP homology 2 domain (30). Recently IRSp53 has been shown to bind to neural isoforms of espin (31), a novel parallel actin bundling protein originally identified as a component of the Sertoli cell spermatid ectoplasmic specialization (32). The resultant multidomain actin bundling protein complexes may bundle F-actin with increased efficiency or contribute to changes in F-actin dynamics. Second, the SH3-mediated interaction could determine the localization of IRSp53. Although we and others (10) have shown that IRSp53 is able to self-localize in filopodia using its N terminus, levels of accumulation appear not to be high. Considering that actin bundling proteins require a relatively high molar ratio to actin to function, this level of specificity may not be sufficient to support dynamic behavior of the cell periphery in nontransfected cells. Both WAVE2 and Mena are shown to localize at the filopodial tip (25, 33, 34), again suggesting the functional redundancy of these protein complexes with increased specificity of localization.

Here we show that the activity of the IMD is tightly regulated by Rac1 and Cdc42, in a manner similar to that of the SH3 domain (4, 7). Our results suggest that the central region of IRSp53, including the half-CRIB motif, is essential for the autoinhibition of the IMD. The N terminus (aa 1–178) of IRSp53 has been shown to interact with the region around the half-CRIB motif and inhibit binding of the SH3 domain to Mena (7). The autoinhibitory mechanisms of the IMD and the SH3 domain may work together within the same molecule. Conversely, F-actin association of the IMD and the SH3 ligand binding are likely to activate or stabilize each other.

We propose that IRSp53 is a direct effecter of Cdc42 and Rac1, acting in concert with various partner proteins recruited by the SH3 domain. Further analyses are required to evaluate the activities of various IRSp53-partner protein complexes and their specific roles in the regulation of cortical actin dynamics. Although MIM has been shown to interact with protein tyrosine phosphatase delta (13), its regulation remains unknown. Our present study reveals that the IMDs are highly conserved both structurally and functionally. So far we have not found any apparent sequence homology of this domain with known F-actin interacting proteins. Future work including crystallographic studies will be needed to ascertain precise molecular mechanisms for F-actin bundling by the IMDs as well as to clarify their regulation, especially by small GTPases in IRSp53.

Acknowledgments—We thank Hiroaki Miki (Institute of Medical Science, Tokyo University, Tokyo) for pEF-BOS-Myc-IRSp53; Masahiko Hibi (Riken Center for Developmental Biology) for Zebrafish cDNA; Michiyuki Matsuda (Research Institute for Microbial Diseases, Osaka University, Suita) for helpful discussion; Manami Sone and Eiko Moriishi for technical assistance; and Hitomi Shimamoto for preparing the manuscript.

REFERENCES

1. Abbott, M. A., Wells, D. G., and Fallon, J. R. (1999) *J. Neurosci.* **19,** 7300–7308
2. Oda, K., Shiratsuchi, T., Nishimori, H., Inazawa, J., Yoshikawa, H., Taketani, Y., Nakamura, Y., and Tokino, T. (1999) *Cytogenet. Cell Genet.* **84,** 75–82
3. Yeh, T. C., Ogawa, W., Danielsen, A. G., and Roth, R. A. (1996) *J. Biol. Chem.* **271,** 2921–2928
4. Miki, H., Yamaguchi, H., Suetsugu, S., and Takenawa, T. (2000) *Nature* **408,** 732–735
5. Takenawa, T., and Miki, H. (2001) *J. Cell Sci.* **114,** 1801–1809
6. Govind, S., Kozma, R., Monfries, C., Lim, L., and Ahmed, S. (2001) *J. Cell Biol.* **152,** 579–594
7. Krugmann, S., Jordens, I., Gevaert, K., Driessens, M., Vandekerckhove, J., and Hall, A. (2001) *Curr. Biol.* **11,** 1645–1655
8. Miki, H., and Takenawa, T. (2002) *Biochem. Biophys. Res. Commun.* **293,** 93–99
9. Alvarez, C. E., Sutcliffe, J. G., and Thomas, E. A. (2002) *J. Biol. Chem.* **277,** 24728–24734
10. Nakagawa, H., Miki, H., Nozumi, M., Takenawa, T., Miyamoto, S., Wehland, J., and Small, J. V. (2003) *J. Cell Sci.* **116,** 2577–2583
11. Lee, Y. G., Macoska, J. A., Korenchuk, S., and Pienta, K. J. (2002) *Neoplasia* **4,** 291–294
12. Mattila, P. K., Salminen, M., Yamashiro, T., and Lappalainen, P. (2003) *J. Biol. Chem.* **278,** 8452–8459
13. Woodings, J. A., Sharp, S. J., and Machesky, L. M. (2003) *Biochem. J.* **371,** 463–471
14. Kelley, L. A., MacCallum, R. M., and Sternberg, M. J. (2000) *J. Mol. Biol.* **299,** 499–520
15. Niwa, H., Yamamura, K., and Miyazaki, J. (1991) *Gene (Amst.)* **108,** 193–199
16. Nagashima, K., Endo, A., Ogita, H., Kawana, A., Yamagishi, A., Kitabatake, A., Matsuda, M., and Mochizuki, N. (2002) *Mol. Biol. Cell* **13,** 4231–4242
17. Spudich, J. A., and Watt, S. (1971) *J. Biol. Chem.* **246,** 4866–4871
18. Svitkina, T. M., Bulanova, E. A., Chaga, O. Y., Vignjevic, D. M., Kojima, S., Vasiliev, J. M., and Borisy, G. G. (2003) *J. Cell Biol.* **160,** 409–421
19. Garrard, S. M., Capaldo, C. T., Gao, L., Rosen, M. K., Macara, I. G., and Tomchick, D. R. (2003) *EMBO J.* **22,** 1125–1133
20. DeRosier, D. J., and Tilney, L. G. (1982) *Cold Spring Harb. Symp. Quant. Biol.* **46,** 525–540
21. Volkmann, N., DeRosier, D., Matsudaira, P., and Hanein, D. (2001) *J. Cell Biol.* **153,** 947–956
22. Bartles, J. R. (2000) *Curr. Opin. Cell Biol.* **12,** 72–78
23. DeRosier, D. J., and Tilney, L. G. (2000) *J. Cell Biol.* **148,** 1–6
24. Small, J. V., Stradal, T., Vignal, E., and Rottner, K. (2002) *Trends Cell Biol.* **12,** 112–120
25. Nozumi, M., Nakagawa, H., Miki, H., Takenawa, T., and Miyamoto, S. (2003) *J. Cell Sci.* **116,** 239–246
26. Vignjevic, D., Yarar, D., Welch, M. D., Peloquin, J., Svitkina, T., and Borisy, G. G. (2003) *J. Cell Biol.* **160,** 951–962
27. Meyer, R. K., and Aebi, U. (1990) *J. Cell Biol.* **110,** 2013–2024
28. Taylor, K. A., Taylor, D. W., and Schachat, F. (2000) *J. Cell Biol.* **149,** 635–646
29. Katoh, K., Kano, Y., Masuda, M., Onishi, H., and Fujiwara, K. (1998) *Mol. Biol. Cell* **9,** 1919–1938
30. Bachmann, C., Fischer, L., Walter, U., and Reinhard, M. (1999) *J. Biol. Chem.* **274,** 23549–23557
31. Sekerkova, G., Loomis, P. A., Changyaleket, B., Zheng, L., Eytan, R., Chen, B., Mugnaini, E., and Bartles, J. R. (2003) *J. Neurosci.* **23,** 1310–1319
32. Bartles, J. R., Wierda, A., and Zheng, L. (1996) *J. Cell Sci.* **109,** 1229–1239
33. Bear, J. E., Svitkina, T. M., Krause, M., Schafer, D. A., Loureiro, J. J., Strasser, G. A., Maly, I. V., Chaga, O. Y., Cooper, J. A., Borisy, G. G., and Gertler, F. B. (2002) *Cell* **109,** 509–521
34. Krause, M., Bear, J. E., Loureiro, J. J., and Gertler, F. B. (2002) *J. Cell Sci.* **115,** 4721–4726

ELSEVIER

Neuroscience Letters 357 (2004) 219–222

Neuroscience Letters

www.elsevier.com/locate/neulet

Temporal and topographic profiles of cyclooxygenase-2 expression during 24 h of focal brain ischemia in rats

Chiaki Yokota[a,*], Tomohito Kaji[b], Yuji Kuge[c], Hiroyasu Inoue[d], Nagara Tamaki[b], Kazuo Minematsu[e]

[a]*Cerebrovascular Laboratory, Department of Pathogenesis, National Cardiovascular Center Research Institute, 5-7-1 Fujishirodai, Suita, Osaka, 565-8565, Japan*

[b]*Department of Nuclear Medicine, Graduate School of Medicine, Hokkaido University, Sapporo, Japan*

[c]*Department of Patho-functional Bioanalysis, Graduate School of Pharmaceutical Sciences, Kyoto University, Kyoto, Japan*

[d]*Division of Molecular Pharmacology, Department of Pharmacology, National Cardiovascular Center Research Institute, Osaka, Japan*

[e]*Cerebrovascular Division, Department of Medicine, National Cardiovascular Center, Osaka, Japan*

Received 6 October 2003; received in revised form 17 December 2003; accepted 26 December 2003

Abstract

Substantial increases in cyclooxygenase-2 (COX-2) mRNA and protein levels were demonstrated in the peri-infarct and focal ischemic areas after 3–24 and 12–24 h, respectively, in rats. In the ischemic core, significant increases in COX-2 mRNA followed 6 h of ischemia, though the peak level was about one-third of that in the peri-infarct area. Increases in COX-2 protein in the ischemic core were not observed during ischemic periods. Diffuse, neuronal COX-2 staining was found in peri-infarct areas as well as in discrete, immunoreactive neurons in the ischemic core. Robust increases in prostaglandin E_2 levels in the peri-infarct area were demonstrated following 24 h of ischemia. Prostaglandin production as well as COX-2 expression in ischemic tissues depended on the degree and duration of the reduction in cerebral blood flow.

Keywords: Cyclooxygenase-2; Focal brain ischemia; Prostaglandin E_2; 6-keto-PG $F_{1\alpha}$; Cerebral blood flow; Rat

Cyclooxygenase-2 (COX-2), a rate-limiting enzyme in prostaglandin synthesis, is rapidly induced by proinflammatory cytokines in vitro and has been shown to mediate the induction of prostaglandin synthesis during the inflammatory response in vivo [17]. Accumulating evidence suggests that inflammatory processes play a role in the development and progression of atherosclerosis [2,8,14] and COX-2 in particular has become the focus of attention as a therapeutic target enzyme in acute coronary syndromes [1] and Alzheimer's disease [16]. We previously reported that neuronal COX-2 was induced within potentially viable hypoperfused brain areas after a 24 h ischemic period in non-human primates [20]. The role of neuronal COX-2 within such peri-infarct areas, however, is still unclear. Several reports using various rodent models suggested that COX-2 played a role in the development of ischemic injury [3,4,12]. A few postmortem reports suggested that the production of prostanoids by COX-2 after acute ischemia could contribute to the remodeling of neural networks that is seen after focal infarction [15]. The objective of the present study was to elucidate the topography and time course of COX-2 expression and prostaglandin (PG) E_2 (the major prostanoid involved in inflammation) production, as well as the production of the prostacyclin metabolite 6-keto-PG $F_{1\alpha}$ [11,13] during 24 h of focal brain ischemia.

Male Sprague–Dawley rats (300–350 g, $n = 40$) were used in this study. All procedures were approved by our Institutional Animal Research Committee and were performed in accordance with the standards published by the National Research Council. Rats were anesthetized with chloral hydrate (400 mg/kg body weight i.p.) and focal brain ischemia was produced by the intraluminal occlusion of the ostium of the right middle cerebral artery with nylon monofilaments, as previously described [7,9]. Rectal temperatures were monitored and maintained at around 37

* Corresponding author. Tel.: +81-6-6833-5012; fax: +81-6-6872-8091.
E-mail address: cyokota@ri.ncvc.go.jp (C. Yokota).

0304-3940/03/$ - see front matter © 2003 Elsevier Ireland Ltd. All rights reserved.
doi:10.1016/j.neulet.2003.12.109

°C with the aid of heating pads. Rats were sacrificed under chloral hydrate anesthesia at time 0 and at different times points after arterial occlusion (1, 2, 3, 4, 6, 8, 12, and 24 h, $n = 4$-5/time point) and their brains immediately immersed in ice-cold saline. The brains were then cut into four coronal sections (blocks A–D) as shown in Fig. 1A. Several blocks were frozen in isopentane-dry ice and stored at − 80 °C until use, whereas others (from C) were embedded in paraffin for immunohistochemistry. Analysis of COX-2 expression (mRNA, protein), and measurement of the concentrations of PGE_2 and the prostacyclin metabolite 6-keto-PG $F_{1\alpha}$ in the peri-infarct areas and the ischemic core were performed using blocks A and C, respectively.

In some animals, *N*-isoproryl-*p*-[^{125}I]-iodoamphetamine ([^{125}I]IMP) (2.22 MBq/kg body weight) was injected into the femoral vein 5 min before sacrifice and ex vivo autoradiography was performed to measure cerebral blood flow (CBF) using blocks B and D. For each frozen block, tissues that were adjacent to block C were serially sectioned (20 μm). Exposure was carried out for 7 days in order to visualize the distribution of [^{125}I]IMP. The autoradiograms were analyzed using a computerized imaging analysis system (Bio-imaging Analyzer BAS-5000, Fuji Photo Film, Tokyo, Japan). A total of four regions of interest (ROIs), as shown in Fig. 1B, were bilaterally and symmetrically positioned in the cerebral cortices in each coronal slice of blocks B and D. Asymmetry indices (AIs) were defined as the ratios of values for ROIs in the hemisphere ipsilateral to the arterial occlusion (right) to those of the contralateral homologous ROIs. AIs of the ischemic core were defined as a/d, whereas the AIs of the peri-infarct area were defined as b/c (Fig. 1B). An average AI value from blocks B and D was calculated for the CBF in each area of the ischemic core and peri-infarction areas.

RNA preparation and blot analysis were performed using cortices from blocks A (peri-infarct area) and C (ischemic core) as previously described [6]. For the immunoblot analyses, right cortical samples from block A (peri-infarct area) were obtained from each animal at time 0, and 3, 6, 12, and 24 h after ischemia ($n = 4$-5 for each period). The sample volumes, which were about 20 mg for each animal, were pooled together for each ischemic period. Right

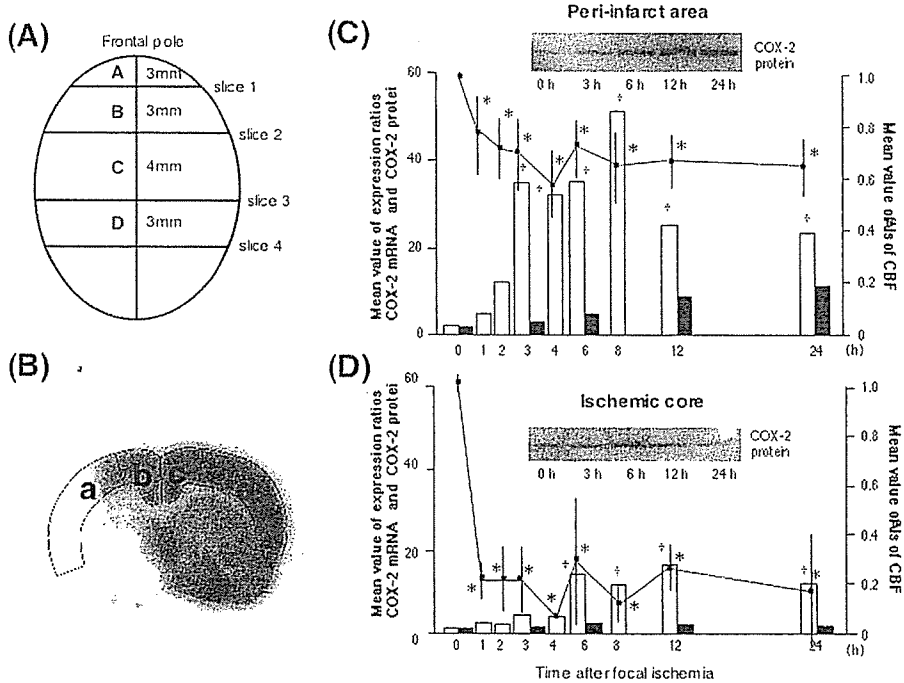

Fig. 1. Temporal profile of COX-2 expression associated with changes in CBF during 24 h of ischemia. (A) The brain was stereotaxically divided, on ice, into four coronal sections using a brain matrix. The first slice was made 3 mm from the frontal pole (block A), while the other three were cut at 3 mm (block B), 7 mm (block C), and 10 mm (block D) intervals posterior to the first slice. Determination of COX-2 expression levels (mRNA, protein) in the peri-infarct area and ischemic core was performed using blocks A and C, respectively. (B) To measure CBF in each animal, four regions of interest (ROIs) were bilaterally symmetrically placed on the cerebral cortices using coronal frozen slices from blocks B and D. Asymmetry indices (AIs) of the ischemic core were defined as a/d, whereas the AIs of the peri-infarct area were defined as b/c. (C,D) Lines indicate the mean AI values of CBF. The open and solid columns correspond to the mean expression ratios of COX-2 mRNA and COX-2 protein, respectively. Figures C and D show the time course of COX-2 expression in the peri-infarct area and ischemic core, respectively. A one-way ANOVA and post-hoc Fisher's tests were used to assess the differences in AIs and expression ratios of COX-2 mRNA between the different ischemic time points. CBF values in the peri-infarct area and ischemic core were significantly reduced compared to controls immediately after arterial occlusion ($^*P < 0.05$). The mean CBF values in the ischemic core and peri-infarct area were 0.19 ± 0.07 (mean ± SD) and 0.67 ± 0.06, respectively. The time course of COX-2 expression in the peri-infarct area was different from that in the ischemic core. Thus, the expression ratios of COX-2 mRNA increased significantly after 3 h of ischemia ($^\dagger P < 0.05$), with COX-2 protein also increasing with time in the peri-infarct area. On the other hand, significant increases in COX-2 mRNA were found 6 h after ischemia ($^\dagger P < 0.05$), and increases in COX-2 protein were not observed during the ischemic period in the ischemic core.

cortical samples from block C (ischemic core) for each ischemic period were also pooled together in this manner. Immunoblot analyses were then performed on each pooled sample as previously described [19]. COX-2 expression (mRNA, protein) in the ischemic cortices was calculated as expression ratios, defined as the ratio of the COX-2 mRNA or protein signals in the ischemic samples to their mean values in the corresponding control areas.

For immunohistochemistry, a mirror sectioning technique was used to colocalize COX-2 and microtubule-associated protein 2 (MAP-2), a neuronal skeletal protein, in sections from block C as previously described [19]. Negative controls consisted of sections that were incubated overnight without the primary antibody and processed as above.

Tissue concentrations of PGE_2 and 6-keto-PG $F_{1\alpha}$ in the right (ischemic) cortices of blocks A (peri-infarct area) and C (ischemic core) were determined using radioimmunoassay kits (Perkin-Elmer Life Sciences, Inc. MA, USA), and values were normalized for protein content.

Significant reductions in AIs for CBF in the peri-infarct area and ischemic core were demonstrated in animals at each ischemic time point compared to controls (Fig. 1C,D). The expression ratios of COX-2 mRNA increased significantly between 3 and 24 h of ischemia in the peri-infarct area compared to controls (Fig. 1C). In the ischemic core, significant increases in COX-2 mRNA were seen following 6 h of ischemia, which remained through 24 h (Fig. 1D). The peak value of the expression ratio of COX-2 protein in the peri-infarct area was 10.7 at 24 h of ischemia, while the peak expression ratio in the ischemic core was 2.0 at 6 h of ischemia.

COX-2 immunoreactive neurons were found predominantly in the peri-infarct area, though elevations in the immunohistochemical staining of discrete neuronal populations were also observed in the ischemic core (Fig. 2). Both COX-2 and MAP-2 immunoreactivity were abolished when the primary antibody was omitted.

Although no significant increases in PGE_2 and prostacyclin levels were observed in the peri-infarct and ischemic core areas following 3 h of ischemia, significant increases in prostaglandin levels were found in the ischemic hemisphere

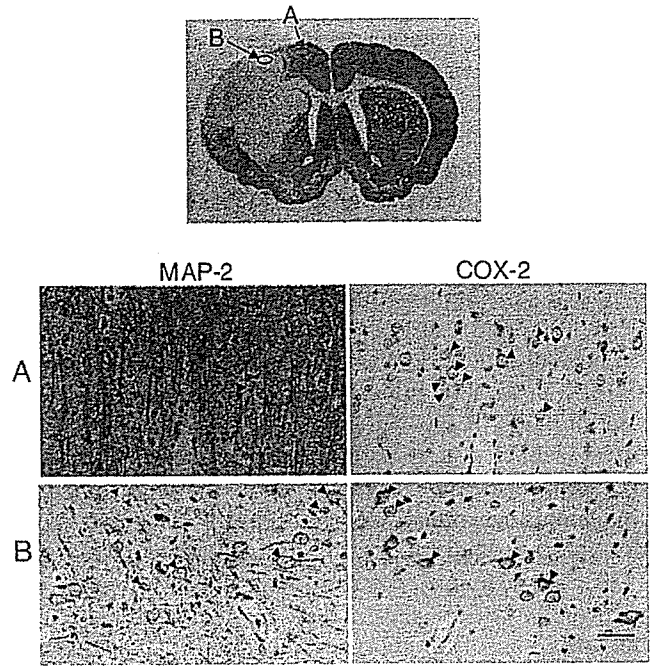

Fig. 2. Immunohistochemical analysis of COX-2. The single top figure shows a coronal slice of the brain of an animal that had undergone 3 h of ischemia, which was immunostained for microtubule-associated protein 2 (MAP-2). The bottom figures are sections that were immunostained for COX-2 and MAP-2 that were derived from either the peri-infarct area (region A in the top figure) or the ischemic core (B). Immunoreactive COX-2 and MAP-2 were localized in the same neurons in the ischemic core and peri-infarct area (arrow heads). Scale bar: 100 μm.

following 24 h of ischemia. In particular, PGE_2 levels in the peri-infarct area increased significantly (Table 1).

We previously demonstrated, in a small number of non-human primates, that post-ischemic COX-2 expression was regulated by the extent of CBF reduction [20]. In the present study, serial changes in the expression of COX-2 during focal ischemia were evaluated more closely in relation to the degree and duration of CBF reduction, and COX-2 reaction products (PGE_2 and prostacyclin), which were not analyzed in our previous study, were also examined. The time course of COX-2 expression in the ischemic core, characterized by a CBF of <20% of baseline values, was different from that seen in the peri-infarct area, where 70–80% of control CBF was observed following 24 h of ischemia. The upregulation

Table 1
Prostaglandin production (pg/mg total protein) in the right (ischemic) hemisphere

Prostaglandin	Duration of ischemia (h)	Peri-infarct area	Ischemic core
PGE_2	0	60.8 ± 16.6	21.4 ± 11.4
	3	156.6 ± 70.1	54.4 ± 22.3
	24	2609.0 ± 2522.0*†	414.6 ± 226.3*†
Prostacyclin metabolite (6-keto-PG $F_{1\alpha}$)	0	122.3 ± 47.6	47.6 ± 23.0
	3	200.8 ± 59.7	93.4 ± 43.5
	24	1143.0 ± 623.7*†	341.6 ± 84.5*†

*$P < 0.05$ vs. 0 h (control); †$P < 0.05$ vs. 3 h ischemia by ANOVA. The values are the mean ± SD.

of COX-2 mRNA in the peri-infarct area persisted for at least 24 h after ischemia, as did the production of COX-2 protein, which led to significant increases in prostacyclin as well as PGE_2 levels following 24 h of ischemia. In the ischemic core, increases in COX-2 mRNA persisted during the 24 h of ischemia, though significant increases in COX-2 protein were not observed. This latter finding was considered to be due to the severe ischemic injury that was caused by reduced CBF, which likely affected protein synthesis [5]. This assertion is supported by the work of Xie et al. [18] who reported that a CBF of $<70\%$ of controls suppressed protein synthesis. In spite of these effects on COX-2 protein, significant increases were seen in the concentration of prostaglandins in the ischemic core 24 h after ischemia. Local increases in neuronal COX-2 expression in the ischemic core, as determined by immunohistochemical analysis, could have accounted for this increase in prostaglandin concentration. Increases in PGE_2 in ischemic cortices after 24 h of ischemia, particularly in peri-infarct areas, were probably due to the upregulation of membrane-associated PGE_2 synthase (mPGES) activity as well as the induction of COX-2, which were reported to be essential components for delayed PGE_2 biosynthesis [10].

The induction of neuronal COX-2 is important for the regulation of prostaglandin signaling in post-ischemic regions, and the magnitude of COX-2 activity and prostaglandin production is determined by the degree and duration of CBF reduction. Before novel therapeutic options for stroke patients can be developed, further clarification of the effects of COX-2 during and after ischemia will be required.

Acknowledgements

This study was supported in part by a Grant-in-Aid for Scientific Research from the Japan Society for the Promotion of Science, by grants from the Takeda Medical Research Foundation, by the Mitsubishi Pharma Research Foundation, and by the Japan Heart Foundation.

References

[1] R. Altman, H.L. Luciardi, J. Muntaner, F.D. Rio, S.G. Berman, R. Lopez, C. Gonzalez, Efficacy assessment of meloxicam, a preferential cyclooxygenase-2 inhibitor, in acute coronary syndromes without ST-segment elevation: the Nonsteroidal Anti-Inflammatory Drugs in Unstable Angina Treatment-2 (NUT-2) pilot study, Circulation 106 (2002) 191–195.

[2] F.C. Barone, G.Z. Feuerstein, Inflammatory mediators and stroke: new opportunities for novel therapeutics, J. Cereb. Blood Flow Metab. 19 (1999) 819–834.

[3] Y. Collaco-Moraes, B. Aspey, M. Harrison, J. de-Belleroche, Cyclo-oxygenase-2 messenger RNA induction in focal cerebral ischemia, J. Cereb. Blood Flow Metab. 16 (1996) 1366–1372.

[4] K. Hara, D.L. Kong, F.R. Sharp, P.R. Weinstein, Effect of selective inhibition of cyclooxygenase 2 on temporary focal cerebral ischemia in rats, Neurosci. Lett. 256 (1998) 53–56.

[5] K.A. Hossmann, Viability thresholds and the penumbra of focal ischemia, Ann. Neurol. 36 (1994) 557–565.

[6] H. Inoue, C. Yokoyama, S. Hara, Y. Tone, T. Tanabe, Transcriptional regulation of human prostaglandin-endoperoxide synthase-2 gene by lipopolysaccharide and phorbol ester in vascular endothelial cells, J. Biol. Chem. 270 (1995) 24965–24971.

[7] Y. Kuge, K. Minematsu, T. Yamaguchi, Y. Miyake, Nylon monofilament for intraluminal middle cerebral artery occlusion in rats, Stroke 26 (1995) 1655–1658.

[8] P.L. McGeer, M. Schulzer, E.G. McGeer, Arthritis and anti-inflammatory agents as possible protective factors for Alzheimer's disease: a review of 17 epidemiologic studies, Neurology 47 (1996) 425–432.

[9] K. Minematsu, L. Li, M. Fisher, C.H. Sotak, M.A. Davis, M.S. Fiandaca, Diffusion weighted magnetic resonance imaging: rapid and quantitative detection of focal brain ischemia, Neurology 42 (1992) 235–240.

[10] M. Murakami, H. Naraba, T. Tanioka, N. Semmyo, Y. Nakatani, F. Kojima, T. Ikeda, M. Fueki, A. Ueno, S. Oh-ishi, I. Kudo, Regulation of prostaglandin E2 biosynthesis by inducible membrane-associated prostaglandin E2 synthase that acts in concert with cyclooxygenase-2, J. Biol. Chem. 275 (2000) 32783–32792.

[11] T. Murata, F. Ushikubi, T. Matsuoka, M. Hirata, A. Yamasaki, Y. Sugimoto, A. Ichikawa, Y. Aze, T. Tanaka, N. Yoshida, A. Ueno, S. Oh-ishi, S. Narumiya, Altered pain perception and inflammatory response in mice lacking prostacyclin receptor, Nature 388 (1997) 678–682.

[12] S. Nogawa, F. Zhang, M.E. Ross, C. Iadecola, Cyclo-oxygenase-2 gene expression in neurons contributes to ischemic brain damage, J. Neurosci. 17 (1997) 2746–2755.

[13] J.P. Portanova, Y. Zhang, G.D. Anderson, D.D. Hauser, J.L. Masferrer, K. Seibert, S.A. Gregory, P.C. Isakson, Selective neutralization of prostaglandin E2 blocks inflammation, hyperalgesia, and interleukin 6 production in vivo, J. Exp. Med. 184 (1996) 883–891.

[14] R. Ross, Atherosclerosis – an inflammatory disease, N. Engl. J. Med. 340 (1999) 115–126.

[15] T. Sairanen, A. Ristimaki, M.-L. Karjalainen-Lindsberg, A. Paetau, M. Kaste, P.J. Lindsberg, Cyclooxygenase-2 induced globally in infarcted human brain, Ann. Neurol. 43 (1998) 738–747.

[16] C. Scali, M.G. Giovannini, C. Prosperi, A. Bellucci, G. Pepeu, F. Casamenti, The selective cyclooxygenase-2 inhibitor rofecoxib suppresses brain inflammation and protects cholinergic neurons from excitotoxic degeneration in vivo, Neuroscience 117 (2003) 909–919.

[17] D.A. Willoughby, A.R. Moore, P.R. Colville-Nash, COX-1, COX-2, and COX-3 and the future treatment of chronic inflammatory disease, Lancet 355 (2000) 646–648.

[18] Y. Xie, G. Mies, K.A. Hossmann, Ischemic threshold of brain protein synthesis after unilateral carotid artery occlusion in gerbils, Stroke 20 (1989) 620–626.

[19] C. Yokota, H. Inoue, Y. Kuge, T. Abumiya, M. Tagaya, Y. Hasegawa, N. Ejima, N. Tamaki, K. Minematsu, Cyclooxygenase-2 expression associated with spreading depression in a primate model, J. Cereb. Blood Flow Metab. 23 (2003) 395–398.

[20] C. Yokota, Y. Kuge, H. Inoue, M. Tagaya, G. Kito, T. Susumu, N. Tamaki, K. Minematsu, Post-ischemic cyclooxygenase-2 expression is regulated by the extent of cerebral blood flow reduction in non-human primates, Neurosci. Lett. 341 (2003) 37–40.

Neuronal cyclooxygenase-2 expression during spreading depression and focal brain ischemia

Chiaki Yokota[1,3], Yuji Kuge[2], Yasuhiro Hasegawa[3], Hiroyasu Inoue[4], Masafumi Tagaya[5], Takeo Abumiya[6], Go Kito[7], Nagara Tamaki[8] and Kazuo Minematsu[3]

Abstract

In order to clarify the pathophysiology of ischemic stroke, we examined a primate model eliciting SD, a primate thromboembolic model, and a rat model of focal brain ischemia. Immediately after the first SD, focal cortical hyperemia was demonstrated without being followed by spreading or persistent hypoperfusion. Cyclooxygenase-2 (COX-2) induction was detected in SD monkeys by microarray analysis. Immunoreactive neurons were observed in SD animals. In the thromboembolic model, upregulation of COX-2 mRNA expression was observed after 2 h of ischemia, but disappeared by 24 h in the ischemic core. In peri-infarct areas, where flow-metabolism uncoupling was observed, COX-2 expression persisted even after 24 h of ischemia. In focal ischemic rats, diffuse, neuronal COX-2 staining was found in peri-infarct areas as well as in discrete, immunoreactive neurons in the ischemic core. Robust increases in prostaglandin E_2 levels in the peri-infarct areas were demonstrated following 24 h of ischemia. In conclusion, neuronal COX-2 induction was observed in SD animals as well as within potentially viable hypoperfused brain areas. COX-2 expression and prostaglandin production in ischemic tissues depended on the degree and duration of the reduction in cerebral blood flow.

Key words: spreading depression, focal brain ischemia, cyclooxygenase 2, cerebral blood flow

1. Introduction

Cortical spreading depression (SD)[1] has been suggested to play a significant role in the development of ischemic injury under conditions of focal brain ischemia in rat models[2,3]. As proposed by the Stroke Therapy Academic Industry Roundtable[4], nonhuman primate studies are required to clarify the pathophysiology of ischemic stroke, and to verify the safety and efficacy of newly developed drugs that show promising results in rodents. In order to investigate the pathophysiology of acute ischemic stroke, we have developed a primate model eliciting SD and a primate thromboembolic stroke model.

Cyclooxygenase-2 (COX-2), a rate-limiting en-

[1]Cerebrovascular Laboratory, [4]Department of Pharmacology, Research Institute, and [3]Cerebrovascular Division, National Cardiovascular Center
[2]Department of Patho-functional Bioanalysis, Graduate School of Pharmaceutical Sciences, Kyoto University, [5]National Osaka Medical Hospital, [6]Hokkaido Ebetsu Hospital, [7]Shin Nippon Biomedical Laboratories, Ltd., [8]Department of Nuclear Medicine, Graduate School of Medicine, Hokkaido University
5-7-1 Fujishirodai, Suita, Osaka, 565-8565, JAPAN

zyme in prostaglandin synthesis, was induced associated with either eliciting SD or focal brain ischemia in the cortex ipsilateral to the SD elicitation or brain ischemia in the nonprimate cortex[5]. Therefore we examined COX-2 expression and its reaction products during SD and focal brain ischemia in primates as well as rats.

All procedures in this study were approved by our Institutional Animal Research Committee and were performed in accordance with the standards published by the National Research Council (Guide for the Care and Use of Laboratory Animals).

2. Material and methods

2. 1. Spreading depression in a primate model

We used nine adult, male cynomolgus monkeys. Animals were anesthetized with pentobarbital (0.1 mg/kg, i.p.). Anesthesia was maintained with a N_2O/O_2 (70% : 30%) gas mixture inhalation under artificial ventilation through an experimental period. They were divided into 2 groups, such as normal control (group C, n = 3) and SD evoked animals (group SD, n = 6).

SD was elicited by applying 3.3 mol/L potassium chloride (KCl) through a burr hole made in the left parietal skull[6]. Two other burr holes were made rostral to the hole for KCl application. DC potentials were monitored with microelectrodes inserted into the cortex to a depth of 1 mm through the burr holes except the hole for KCl application.

Cerebral blood flow (CBF) was measured with PET and the ^{15}O-labeled water bolus injection method. A baseline CBF measurement was done once prior to application of KCl solution. CBF measurements were repeated 5 times, beginning 3 minutes after the first SD at intervals of approximately 15 minutes. After completion of the PET studies (at 120 min after KCl application), the brain tissues in the group SD were quickly removed after exsanguination following perfusion with cold saline. Samples of brain tissues in the group C were also obtained as the same manner as those in the group SD. We investigated the gene expression profile associated with SD by a cDNA array system containing 9,182 human elements, which was confirmed by RNA blot, immunoblot, and immunohistochemical analyses[7].

2. 2. Thromboembolic stroke model in primates

Thromboembolic stroke was produced in male cynomolgus monkeys (n = 4) as described previously[8]. CBF was measured with ^{15}O-labeled water before and 1, 2, 4, 6, and 24 hours after embolization. Cerebral glucose metabolic rate (CMRglc) was measured with [^{18}F] FDG methods 24 hours after embolization[9]. Lesion size and location 24 hours after embolization was determined by the 2, 3, 5-triphenyl-tetrazolium chloride (TTC) staining method.

For biochemical analyses for brain tissues in thromboembolic stroke model, we used 9 adult male cynomolgus monkeys ; 3 monkeys were served as normal control and the remaining 6 were as ischemic animals[10]. Two hours after a single autologous blood clot injection in 3 monkeys or after the completion of the PET studies in the other monkeys with 24 h-ischemia, brain tissues were perfused with cold saline and the animals were sacrificed. Three normal controls were also sacrificed as the same manner. Expression ratios of COX-2 mRNA were calculated as ratios of COX-2 mRNA against those of normal brains. Cell injury was evaluated by incorporation of digoxigenin deoxy-uridine-5'-triphosphate (dUTP) with the use of DNA polymerase I.

2. 3. Focal brain ischemia in rats

Male Sprague-Dawley rats (300-350 g, n = 40) were used. Focal brain ischemia was produced by the intraluminad occlusion of the ostium of the right middle cerebral artery with nylon monofila-

ments, as previously described[11]. Rats were sacrificed at time 0 and at different times points after arterial occlusion (1, 2, 3, 4, 6, 8, 12, and 24 h, n = 4-5/time point) and their brains immediately immersed in ice-cold saline. Several blocks were frozen in isopentane-dry ice and stored at −80℃ until use, whereas others were embedded in paraffin for immunohistochemistry. Analysis of COX-2 expression (mRNA, protein), and measurement of the concentrations of PGE_2 and the prostacyclin metabolite, 6-keto-$PGF_{1\alpha}$ in the peri-infarct areas and the ischemic core were performed. In some animals, N-isoproryl-*p*-[^{125}I]-iodoamphetamine ([^{125}I]IMP) (2.22 MBq/kg body weight) was injected into the femoral vein 5 min before sacrifice and *ex-vivo* autoradiography was performed to measure cerebral blood flow (CBF) as described previously[12].

3. Results

3. 1. SD in primates

SD waves were recorded in eight of the 9 monkeys. Single episode in three monkeys, twice in two, and six episodes in one were recorded in the rostral sites. In two of three animals with the caudal hole, one had eight episodes and another did once in the caudal sites for chemical stimulation while they did no SD waves in the rostral sites. The remaining one had twice episodes in the rostral and six episodes in the caudal sites. Focal hyperemia was demonstrated adjacent to the site of KCl application immediately after the first SD. Average cortical CBF in the ipsilateral hemisphere increased significantly immediately after the chemical stimulation ($p < 0.05$ by paired t-test), and the significant increase in CBF persisted throughout the experimental period of 2 hours. In the contralateral hemisphere, no significant changes in CBF were observed.

As a result of microarray analysis, increases in normalized signals of gene expression above 1.5-fold was cyclooxygenase-2 (COX-2) gene (1.6-fold), and signal levels in 265 genes were different by at least 1.3-fold between the 2 groups. COX-2 induction was confirmed by RNA blot, immunoblot, and immunohistochemical analyses. Intense immunoreactive neurons were induced in the animals with SDs.

3. 2. Focal brain ischemia in primates

CBF in the temporal cortex and the basal ganglia decreased to < 40% of the contralateral values 1 hour after embolization, following further decline in CBF as well as CMRglc at 24 hour of ischemia. These regions were consistently unstained with TTC, being indicated that both temporal cortex and basal ganglia ipsilateral to the arterial embolization were regarded as the ischemic core. While CBF was > 40% of the contralateral values 1 hour after the embolization and recovered gradually with time in the parietal cortex ipsilateral to the embolization. No obvious TTC-unstained lesions were demonstrated in these regions, implicated that the parietal cortex ipsilateral to the embolization was regarded as the ischemic penumbra. Increased in CMRglc at 24 hours of ischemia compared with those in the contralateral regions, an uncoupling of CBF and CMRglc, were demonstrated in these regions.

The upregulation of COX-2 mRNA expression was observed at 2 h (expression ratio was 7.4), but disappeared by 24 h in the ischemic temporal cortex, where cell injury was apparent by incorporation of dUTP. In the ischemic parietal cortex, where flow-metabolism uncoupling was observed, COX-2 mRNA was persistently induced even at 24 h after ischemia (expression ratio was 4.7), and few damaged cells could be detected by incorporation of dUTP as well as in each region from the hemisphere contralateral to the clot injection. Intense COX-2 immunoreactivity was found in discrete neurons in the ischemic parietal

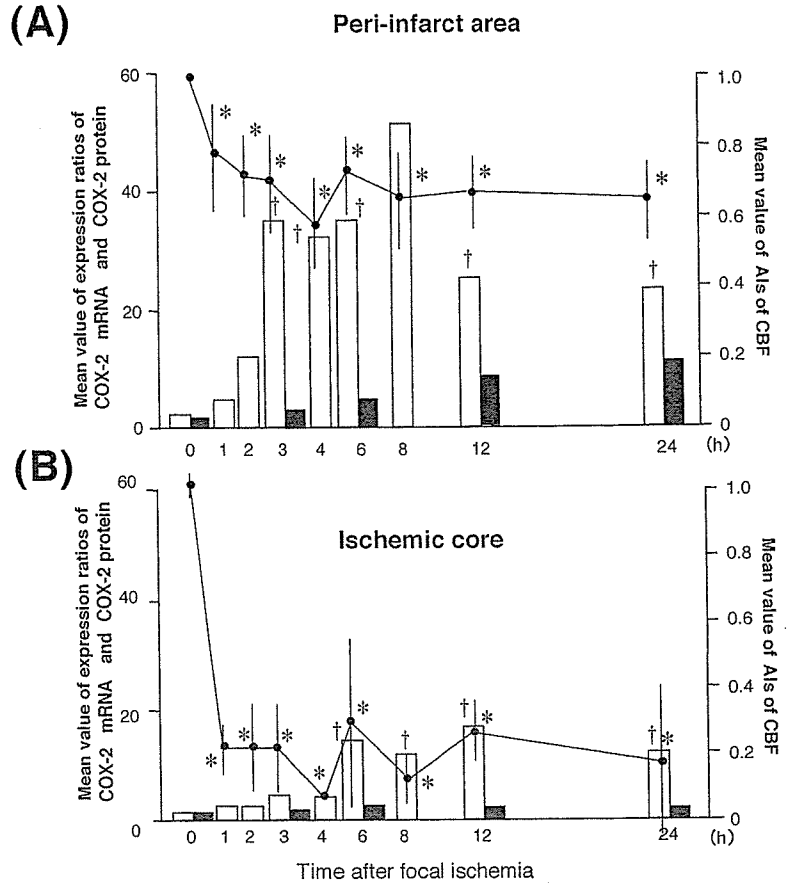

Fig. 1. Temporal profile of COX-2 expression associated with changes in CBF during 24 h of ischemia

Lines indicate the mean asymmetry index (AI) values of CBF. The open and solid columns correspond to the mean expression ratios of COX-2 mRNA and COX-2 protein, respectively. Figures A and B show the time course of COX-2 expression in the peri-infarct areas and ischemic core, respectively. A one-way ANOVA and post-hoc Fisher's tests were used to assess the differences in AIs and expression ratios of COX-2 mRNA between the different ischemic time points. CBF in the peri-infarct areas and ischemic core were significantly reduced compared to controls immediately after arterial occlusion (*: $p<0.05$). The mean CBFs in the ischemic core and peri-infarct areas were 0.19 ± 0.07 (mean ± SD) and 0.67 ± 0.06, respectively. The time course of COX-2 expression in the peri-infarct areas was different from that in the ischemic core. Thus, the expression ratios of COX-2 mRNA increased significantly after 3 h of ischemia (†: $p<0.05$), with COX-2 protein increasing with time in the peri-infarct areas. On the other hand, significant increases in COX-2 mRNA were found 6 h after ischemia (†: $p<0.05$), and increases in COX-2 protein were not observed during the ischemic period in the ischemic core.

cortex, although no significant increases in COX-2 protein level were shown either in the ischemic temporal or parietal cortices.

3. 3 Focal brain ischemia in rats